AD-A252 007 ②

REPORT DOCUMENTATION PAG

1. Agency Use Only *(Leave blank).*

2. Report Date.
1992

3. Report Type and Dates Covered.
Final - Contractor Report

4. Title and Subtitle.
Artificial Corrosion of Cu-alloys - A contribution to Understanding Microbial and Nonmicrobial Sulfide Corrosion

5. Funding Numbers.

Contract	N00014-90-J-6010
Program Element No.	0601153N
Project No.	00101
Task No.	109
Accession No.	DN250162
Work Unit No.	93330F

6. Author(s).
Dr. Terri L. Woods*

DTIC
ELECTE
JUN 23 1992
S C D

7. Performing Organization Name(s) and Address(es).
*East Carolina University
Greenville, N.C. 27858-4353

8. Performing Organization Report Number.

9. Sponsoring/Monitoring Agency Name(s) and Address(es).
Naval Oceanographic and Atmospheric Research Laboratory
Ocean Science Directorate
Stennis Space Center, MS 39529-5004

10. Sponsoring/Monitoring Agency Report Number
CR 022:92

11. Supplementary Notes.

12a. Distribution/Availability Statement.
Approved for public release; distribution is unlimited.

92-16272

13. Abstract *(Maximum 200 words).*

90 Cu-10Ni wafers were corroded abiotically in synthetic seawater solutions containing various concentrations of H^+, dissolved O_2, and dissolved sulfide. The samples were not disturbed during the corrosion process by stirring or monitoring of the solution chemistry. The Eh, pH, and the concentrations of dissolved O_2 and sulfide in the initial and final solutions were measured. Upon removal, the corroded wafers were analyzed by SEM, EDX, XPS, and electron microprobe. These analyses revealed the presence of chalcocite, paratcamite, cuprite, aragonite, and possible djurleite and digenite on the surfaces of the wafers. Adherence of the corrosion films varied with solution chemistry from those that were nonadherent to those showing good adherence. Copper and nickel behaved very differently during the experiments. The data suggest a model for this abiotic corrosion process that involves rapid scavenging of dissolved sulfide by copper to form an amorphous or cryptocystalline Cu-S phase which later recrystallizes into large, well-formed Cu-S minerals. The Cu-S minerals initially formed under reducing conditions existed even after the solutions become quite oxidizing.

14. Subject Terms.
Biofouling, corrosion, biodeterioration, electrochemistry

15. Number of Pages.
37

16. Price Code.

17. Security Classification of Report. Unclassified	**18. Security Classification of This Page.** Unclassified	**19. Security Classification of Abstract.** Unclassified	**20. Limitation of Abstract.** SAR

NSN 7540-01-280-5500

Standard Form 298 (Rev. 2-89)
Prescribed by ANSI Std. Z39-18
298-102

92 6 18 046

Final Report for Research Conducted
under Contract # N00014-90-J-6010

Department of the Navy
Naval Oceanographic and Atmospheric Research Laboratory
Code 102:RDS Stennis Space Center, MS 39529-5004

Artificial Corrosion of Cu-alloys - A contribution to Understanding Microbial and Nonmicrobial Sulfide Corrosion

Dr. Terri L. Woods
East Carolina University
Department of Geology
Greenville, NC 27858-4353

ABSTRACT

90Cu-10Ni wafers were corroded abiotically in synthetic seawater solutions containing various concentrations of H^+, dissolved O_2, and dissolved sulfide. The samples were not disturbed during the corrosion process by stirring or monitoring of the solution chemistry. The Eh, pH, and the concentrations of dissolved O_2 and sulfide in the initial and final solutions were measured. Upon removal, the corroded wafers were analyzed by SEM, EDX, XPS, and electron microprobe. These analyses revealed the presence of chalcocite, paratacamite, cuprite, aragonite, and possibly djurleite and digenite on the surfaces of the wafers. Adherence of the corrosion films varied with solution chemistry from those that were nonadherent to those showing good adherence. Copper and nickel behaved very differently during the experiments. The data suggest a model for this abiotic corrosion process that involves rapid scavenging of dissolved sulfide by copper to form an amorphous or cryptocrystalline Cu-S phase which later recrystallizes into large, well-formed Cu-S minerals. The Cu-S minerals initially formed under reducing conditions persisted even after the solutions became quite oxidizing.

INTRODUCTION

Exposure of metal alloys to seawater containing excessive concentrations of sulfide can cause accelerated corrosion.[1] Unusually high concentrations of reduced sulfide species result from pollution of harbor waters by city sewage outfalls, industrial waste discharge, rotting vegetation, and from the activity of sulfate-reducing bacteria (SRB). Such accelerated corrosion of copper piping on vessels can eventually lead to premature failure.[2-4]

Many researchers have studied the effects of pH and oxygen and sulfide concentrations on corrosion rates of copper alloys in natural and synthetic seawaters.[5-8] Eiselstein et al.[4] established that the presence of both sulfide and oxygen in seawater results in very high corrosion rates. Even in the complete absence of oxygen, however, the presence of sulfide in seawater leads to an increase in corrosion rates.[7]

Copper-sulfide films formed in oxygenated, sulfide-polluted seawater do not provide protection against further corrosion. Previous studies[1,4] have suggested that the formation of a porous copper - sulfide film inhibits the natural growth of a protective cuprous oxide film. Also, Syrett[3] suggests that a film of heterogeneous mineralogy, no matter how adherent, may be porous enough to permit corroding ions to pass through to the copper alloy. Chalcocite has been identified as a non-protective corrosion product[7], whereas, djurleite, may produce a protective film.[8]

Sulfate-reducing bacteria may accelerate corrosion of alloys, and formation of many sulfide films may require SRB.[10-13] In most instances SRB are the most important source of reduced sulfur species.[10] Sulfate-reducing bacteria, use sulfates to produce HS^-, H_2S, polysulfides (SS^{2-}, S_2S^{2-}, S_3S^{2-}, and S_4S^{2-}), minor concentrations of S^{2-}, and colloidal sulfur. These reduced sulfur species enhance conversion of native copper to copper-sulfide minerals.[14] Baas-Becking and Moore[13] have produced digenite, chalcocite and covellite by SRB-induced corrosion of copper. North and MacLeod[11] report the occurrence of chalcocite, covellite, digenite, djurleite and anilite on copper artifacts submerged in seawaters containing SRB. More recently, McNeil et al.[10] produced both monoclinic and hexagonal chalcocite, digenite, djurleite, anilite and minor amounts of covellite in experiments involving SRB. Their tests confirmed that all SRB-induced corrosion of copper and Cu-alloys produce chalcocite, and suggested that other minerals are produced under more specialized conditions.

Most of the previous experimental work has concentrated on the rate of corrosion and the chemistry and adherence of the corrosion products. [Table 1 contains the mineral names, chemical formulae, crystal habits, and crystal systems of many common copper corrosion products.] Very little attention has been paid to the mineralogy and morphology of the corrosion products. Many previous investigations have employed flow-through apparatus or continuous stirring of experimental solutions.[1,3,5-7,9] These experimental conditions are not conducive to the formation of large, well-formed crystals.

Tiny, poorly-formed crystals hinder description of the morphology of individual corrosion products and determination of their interrelationships.

Two papers previously mentioned did describe the mineralogy of the corrosion film. MacDonald et al.[7] reported orthorhombic Cu_2S, which they called chalcocite, cubic Cu_2S, and substoichiometric cuprous sulfide ($Cu_{1.80}S$), but they did not clearly differentiate their mineralogies. They corroded their copper samples in three deoxygenated solutions with different concentrations of dissolved sulfide. Mor and Beccaria [5] conducted X-ray diffraction analysis of their corrosion products which were formed under a wider variety of conditions than those of MacDonald et al.[7] They did not, however, present any SEM analysis of their samples, nor did they report which minerals were verified by X-ray.

The objectives of this investigation were to gain a clearer understanding of the chemistry, texture, mineralogy and adherency of corrosion products formed abiotically on 90Cu-10Ni alloy in seawater of varying pH and dissolved sulfide and oxygen concentrations. In the present study samples were allowed to corrode undisturbed in sulfide-rich seawater solutions in order to enhance the formation of well-crystallized minerals. Experiments such as these also permit a more accurate assessment of the changes in solution chemistry that accompany the corrosion process. The mineralogy, chemistry and texture of the minerals formed on the wafers were investigated by Energy Dispersive X-ray Analysis (EDX), Scanning Electron Microscopy (SEM), X-ray Photoelectron Microscopy (XPS), reflected light microscopy, and electron microprobe.

EXPERIMENTAL PROCEDURES

Synthetic seawater was used as a starting solution for these experiments in order to exclude bacteria from the solutions, and to provide a solution of known and reproducible composition. The seawater was prepared using a modification of the recipe of Lyman and Fleming [15] [revised by Kester et al.[16]] and omitting the $SrCl_2$ $2H_2O$. The pH and salinity of each batch of synthetic seawater was monitored to ensure uniformity. The composition of the experimental solution is given in Table 2.

Eighteen experimental solutions were prepared by combining synthetic seawater with varying concentrations of Na_2S $9H_2O$ (Table 3). Nine of these solutions were aerated solutions containing levels of dissolved oxygen that reflected equilibrium with the atmosphere (7.0 mg/l). The initial Eh value of these solutions, before addition of $Na_2S \cdot 9H_2O$, was 40 mV. After several hours of bubbling with laboratory air to ensure saturation with atmospheric oxygen, various amounts of Na_2S $9H_2O$ were added to these solutions. The pH was then adjusted by addition of HCl to maintain initial pH values between 8.1 and 8.4. Immediately following addition of $Na_2S \cdot 9H_2O$ the Eh of these solutions dropped dramatically and then began to increase. The increase was rapid at first, due to oxidation of dissolved sulfide, but became more gradual as the corrosion reactions proceeded. Initial sulfide concentrations (S^{2-}_T) were varied between 1 and 289 ppm. Such high levels of sulfide were added to encompass the full range of likely chemical conditions. It is difficult to determine what concentrations may exist underneath active biofilms, and sulfide levels may reach this value.

In order to limit the dissolved oxygen to the amounts initially contained in the synthetic seawater, the sample bottles were not opened after the Cu-Ni coupons were added. It was, therefore, not possible to determine the precise Eh values of these solutions as corrosion began. Initial Eh values were later estimated by bubbling synthetic seawater with nitrogen and monitoring Eh values and dissolved oxygen content. When the bubbled solution reached its lowest Eh value various concentrations of $Na_2S \bullet 9H_2O$ were added and Eh values were recorded as the solution chemistry stabilized. Initial Eh values were then estimated by correlating the amount of sulfide added with the associated drop in Eh.

Nine other solutions were prepared inside a nitrogen - filled glove box to create 6 partially-deaerated solutions (0.10 mg/l dissolved oxygen) and 3 deaerated solutions (0.02 mg/l dissolved oxygen). [During preparation of sample 36 the supply of nitrogen gas to the glove box was accidentally cut-off temporarily and the sample, which was originally designated to contain 0.02 mg/l of dissolved oxygen, actually contained 0.10 mg/l of dissolved oxygen.] The initial pH values of the partially-deaerated solutions varied between 7.84 and 8.42, and the initial Eh of the solutions (before addition of $Na_2S\ 9H_2O$) was -130 mV. Initial dissolved sulfide concentrations were varied between 1 and 289 ppm. Initial pH values in the deaerated solutions ranged from 8.07 to 8.36, initial Eh was -170 mV, and initial dissolved sulfide concentrations were varied between 154 and 248 ppm. The Eh of the solutions following addition of $Na_2S \bullet 9H_2O$ was estimated by the procedure described above. Two control solutions, partially deaerated and aerated, were prepared without addition of sulfide. The initial pH and Eh of the partially deaerated solution were 8.40 and -131 mV, respectively. For the aerated control solution the initial pH was 8.40 and the initial Eh was 42 mV.

Two 90Cu-10Ni wafers (1.3 cm^2) were numbered; pretreated by thorough sanding, cleaning and rinsing; and placed in each solution to corrode for approximately 140 days. Electron microprobe analyses of the wafer indicated 87.04-88.19 weight percent (wt. %) Cu, 9.52-10.84 wt. % Ni, 1.15-1.64 wt. % Fe, and 0.26-0.36 wt. % Mn. A semiquantitative EDX spectrum of a wafer is shown in (Figure 1). (The Al peak is due to the Al sample holder.) Copper wafers to be corroded in deaerated and partially deaerated solutions were placed in those solutions immediately after preparation in the glove box.

Samples corroded in aerated solutions were removed under ambient laboratory conditions, rinsed with distilled water, and allowed to air dry. One sample from each bottle was then wrapped in protective paper and placed in a glass bottle to be shipped for XPS analysis. Samples corroded in deaerated and partially-deaerated solutions were removed in the nitrogen-filled glove box, rinsed with distilled water, and allowed to dry in the nitrogen atmosphere. These samples were wrapped in protective paper and sealed in sample vials containing a nitrogen atmosphere before shipment. The second wafer from the solutions was analyzed at East Carolina University by SEM, EDX, X-ray diffractometry, reflected light microscopy, and at the Virginia Polytechnic Institute by electron microprobe.

The pH, Eh, and concentrations of dissolved sulfide and oxygen were determined for the solutions at the beginning and end of the corrosion process (Table 3). Experimental pH and Eh were determined using standard pH and platinum Eh electrodes, and a pH meter. The concentration of dissolved sulfide was determined by titration with lead perchlorate using a Ag-S electrode as an endpoint indicator. Samples of nitrogen-sparged, synthetic seawater were taken during solution preparation, prior to addition of $Na_2S \bullet 9H_2O$. These samples were analyzed for their content of dissolved oxygen using a modified form of the Winkler Iodiometric Titration. Oxygen determinations could not be made following solution preparation because the high concentrations of added sulfide interfere with the titration procedure.

RESULTS

Surface Examinations Using Standard Light Microscopy

To facilitate the identification of corrosion products on the Cu-Ni wafers, specimens were analyzed and described both macroscopically and microscopically. A summary of the macroscopic descriptions is given in Table 4A. Reflected light microscopy did not reveal very much information due to the very fine-grained nature of the thin corrosion film. Chalcocite, and possibly covellite, were tentatively identified by these methods.

Surface Examinations by SEM and EDX

SEM descriptions of the corroded wafers are summarized in Table 4B. SEM photographs and EDX spectra of the significant minerals found on the corroded wafers are shown in Figures 2 - 8. The EDX system was not capable of detecting elements lighter than Na, therefore, oxygen and carbon do not appear in these spectra. Figure 2 is an SEM photograph and EDX spectrum of the lepispherical masses of dipyramidal paratacamite crystals found on samples 2, 4, 20, and the wafer placed in the aerated control solution. Figures 3 and 4 show cuprite cubes and octahedra, respectively, found in samples 2, 4, 10, and 16. Cuprite probably occurs in the inner layers of most samples but was usually covered by subsequent layers of corrosion products. The pseudo-hexagonal, tabular/dipyramidal Cu-S phase [probably mostly chalcocite] found in samples 10, 12 and 24-36 is described in Figure 5, and the serrated Cu-S phase found in samples 10-14 and 26-36 is described in Figure 6. In many samples the underlayer of corrosion product was the platy, porous, layer rich in Cu, S, Ni, and Fe described in Figure 7. The nodular Cu-S phase observed in samples 6, 8, 16, and 22 may be poorly-formed chalcocite (Figure 8).

XPS Analysis

X-ray Photoelectron Spectroscopy (XPS) is a surface analytical technique that provides semi-quantitative to quantitative elemental and chemical state (i.e., oxidation state) information to a depth of approximately 1 nm (100 A) in the sample. [Ion-sputtering (or etching) accessories are available which permit elemental profiling to greater depths.] The technique uses X-rays to stimulate the sample and detects photoelectrons emitted in response. Because these electrons can only travel a short distance before significant energy loss occurs, this technique only samples a very narrow, near-surface region. The minerals occurring in this layer formed in response to the final experimental conditions existing in the solutions (Table 3). These were quite different from the initial levels of oxygen or dissolved sulfide which may have obtained during the first few days or weeks of the 4-month corrosion period. Because there was a significant difference between the initial and final experimental conditions, the mineralogy and chemistry of the bulk of the corrosion film differs considerably from that of the near-surface region in most cases.

Spectra of standard materials are used to calibrate analytical results. Figure 9 is a chemical state plot for the standards analyzed during evaluation of these samples, as well as other values taken from the literature and published databases. It shows kinetic and binding energies useful for identifying the chemical state of sulfur. Characteristics of samples prepared during this study are plotted on Figure 9 and suggest that chalcocite is the dominant corrosion mineral formed on the surface of the Cu-alloy wafers. This suggests that chalcocite was the dominant mineral formed in response to conditions existing near the end of the corrosion experiment. The plot does not exclude the possibility that the bulk of some samples may consist of other Cu-S compounds.

The data plotted on Figure 9 is given in tabular form in Tables 5 and 6 along with some other characteristics of the samples. Tables 7 and 8 provide quantitative information on the surface composition of the samples. This data is for an extremely thin surface layer and, in some cases, may include residues generated by evaporation of small amounts of the synthetic seawater solution that was not rinsed from the samples. The surface chemistry may also have been affected by exposure of the samples to the atmosphere during removal from the solutions and shipment for XPS analysis. As an example, very little sulfur is indicated in Tables 7 and 8 although EDX and microprobe analysis of most samples showed large amounts of sulfur.

Examination of Tables 7 and 8 indicates fairly good correspondence between large atomic percentages of Ca and Cl and the occurrence of aragonite and paratacamite, respectively, on the surfaces of the corroded samples. Some useful information about dealloying of the Cu wafer may also be derivable from these analyses. Aerated samples 6, 8, 16, 10, and 12, as well as, partially deaerated samples 20, 22, 24, and 26 contain significant amounts of Ni in the surface layer compared to other samples. Perhaps the solutions in which these samples formed are especially effective at preferentially leaching Ni from the Cu wafer.

Information acquired during an ion-etching profile of the sample corroded in aerated solution 10 is summarized in Figure 10.

Figure 10A shows the starting points for the three ion-sputtering profiles. In order to perform these the corrosion film was removed from the Cu-alloy wafer in a single layer. Figure 10-B shows the elemental distribution within the top and bottom of the corrosion film, and the top of the Cu-alloy wafer. Each minute of etching corresponds to a sample of approximately 50 A in thickness.

The outermost surface of the corrosion film (far left of plot) shows high levels of O and Cu, and low levels of Ni, Ca, and S, suggesting that the outermost surfaces of the Cu-S minerals observed on this wafer were oxidized. Sulfur levels increase with increasing depth into the corrosion film, and oxygen levels decline. The underside of the corrosion film shows very high levels of Ni and O, and lower levels of S and Cu. Sulfur is seen to reach a peak concentration within the mineral/oxide deposit close to the inner interface. This region is by far the richest in Ni with decreases in Ni, S and Cu observed towards the interface. Oxygen is seen to increase dramatically in this direction. The upper surface of the Cu-alloy wafer exhibits a sudden, dramatic decrease in Ni and increase in Cu, with O and S continuing to change across the interface as they did in the bottom of the corrosion film. The atomic proportions in this layer more closely approach those of tenorite than cuprite. It was apparently overlain by a less-adherent film of mixed Ni, O, S, and Cu, with Ni and S reaching their peaks in this region.

Electron Microprobe Analysis

Samples 14, 22, 30, and 32 were analyzed with a Cameca SX50 electron microprobe for Cu, S, Ni, Fe, Mn, and Cl. Tables 9 and 10 summarize the results of quantitative microprobe analyses of these samples. Table 9 shows representative analyses of minerals which are relatively low in nickel and have the stoichiometry of common copper-sulfide minerals. Table 10 includes data for nickel-rich phases which generally do not show the stoichiometry of a common copper-sulfide. Note also that most of the totals in Table 10 are significantly lower than 100 weight percent (wt. %). This is not a result of selective presentation of data. Almost all of the analyses showing greater than 5 wt. % nickel gave low totals (i.e. < 98 wt.%), and, in general, the phases yielding the lowest totals were the ones richest in nickel.

Figure 11 shows the results of back scatter electron imaging and X-ray element mapping of sample 32. These four figures all represent a cross-section through the corrosion film and upper surface of the alloy wafer. They are all oriented with the alloy wafer to the upper left and the corrosion film to the lower right. The black region in between is mainly epoxy that infiltrated the gap between film and wafer whenever the film peeled away from the alloy. The brightness of various regions in Figure 11A is a complex function of composition. The base of the corrosion film has a distinctly darker coloration suggesting that its composition differs from that of the rest of the film. Analyses from the light-colored region of sample 32 are presented in Table 9 and those from the dark-colored region are given in Table 10.

The X-ray element maps shown in Figures 11B-11D emphasize the zonal distribution of Cu and Ni, and indicate the homogeneous distribution of S. The Ni-rich analyses from samples 30 and 32 given in Table 10 came from dark-colored zones such as that shown in Figure 11A. There was no clear distinction between dark and light zones in sample 14. This zone corresponds to the underside of the corrosion film, which occurs closest to the copper-nickel wafer. Analyses from Table 9 are of the copper-rich, nickel-poor phases in the outer portion of the corrosion film. This elemental distribution mimics that shown on the ion-etching profile of sample 10 (Figure 10). This profile shows very high values for oxygen in the underlayer of the corrosion film. The electron microprobe analyses conducted on these samples were not capable of detecting oxygen, which probably accounts for the low totals recorded for the nickel-rich phases.

The weight percent of Cu, Ni, Fe, Mn, and S in the Cu-S minerals ranged from 75.58-80.14 wt. %, 0.05-4.61 wt. %, 0-0.62 wt. %, 0-0.08 wt. %, and 19.06-20.76 wt. %, respectively. Recalculation of the analyses on the basis of 1 mol of sulfur yielded copper values between 1.847 and 2.08 mols. Analyses from sample 14 indicate a stoichiometry for the copper mineral that correspond to that of chalcocite (Cu_2S). Analyses of samples 30 and 32, however, suggest the possibility that copper-poor minerals such as djurleite ($Cu_{1.96-1.97}S$), digenite ($Cu_{1.75-1.80}S$) or even covellite (CuS) may occur admixed with the chalcocite. Except for covellite, these minerals are virtually indistinguishable from chalcocite with reflected-light microscopy, especially in such thin films as were formed on these wafers. Therefore, it is not possible to determine the interrelationships of these phases. At best, the data provide permissive evidence for the occurrence of djurleite, digenite, and perhaps covellite, especially in sample 30.

Final Chemistry of Solutions

Due to problems with the method selected to measure dissolved oxygen, this parameter was not determined at the conclusion of the corrosion experiment. The deaerated solutions had final dissolved sulfide concentrations of 58, 96, and 160 ppm, indicating a loss of 96, 96, and 88 ppm sulfide, respectively (Table 3). All other experimental solutions contained sulfide concentrations below the detection limit (BDL) of the sulfide electrode (i.e., 10^{-7} M total sulfide).

Final pH values for aerated, partially deaerated and deaerated solutions ranged from 6.70 to 8.40, 6.80 to 8.60, and 8.45 to 8.71, respectively. Final pH values for most solutions were lower than the initial pH. With two exceptions, an increase in pH occurred only in solutions where the initial dissolved oxygen level was 0.02 mg/l (samples 30-34). Those solutions with an initial total sulfide content between 0 and 8 ppm, whether aerated or deaerated, displayed a pH change of no more than 0.4. The partially-deaerated sample with 289ppm ($S^{2-}{}_T$) showed a small decrease in pH (-0.01). The aerated control solution, with no added sulfide, showed no change in pH. The deaerated control showed an increase of 0.20 pH units.

Figure 12 is a graph of the magnitude of the pH change observed in the solution versus the initial dissolved sulfide content of the solution. For initial dissolved sulfide concentrations up to 154 ppm, both the aerated and partially-deaerated solutions showed a decrease in pH and an increase in the magnitude of the pH change with increasing, initial, dissolved sulfide content. The partially deaerated sample that plots well away from the rest of the group is sample 36. Solutions with initial dissolved sulfide concentrations greater than or equal to 154 ppm (with the exception of the aerated solution) showed a much lower increase in the magnitude of the pH change with increased, initial concentration of dissolved sulfide. For the aerated solutions with these high dissolved sulfide levels, the pH decreased as reaction progressed, but for the deaerated solutions, pH increased.

The data displayed in Figure 12 suggest that the magnitude of the change in pH may be a measure of the extent of reaction. If that is the case, the extent of reaction appears to be a strong function of initial sulfide content for solutions with less than 160 ppm sulfide and $0.10 \text{ mg/l} < O_{2(aq)} < 7.0 \text{ mg/l}$. In these solutions higher initial sulfide concentrations may have caused more extensive corrosion to occur. At higher dissolved sulfide levels the extent of reaction does not vary significantly with changes in sulfide content and may, instead, have been limited by oxygen availability. The fact that the low-oxygen, high-sulfide solutions of samples 30-34 contained unreacted dissolved sulfide at the end of the experiment supports this hypothesis.

The aerated solutions can be divided into a high- and low- pH group with initial pH values near 8.40 and 8.15, respectively. The high-pH group (4,8,10,12,14) did not show a good correlation between initial concentration of dissolved sulfide and the magnitude of the change in pH observed, but it did show a good correlation between increasing concentration of dissolved sulfide and decreasing final Eh. The exception is the control solution, which had no added sulfide. The low-pH group (2,6,16) showed a good correlation between initial concentration of dissolved sulfide and the magnitude of the change in pH observed, but showed a virtually constant final Eh.

The partially-deaerated solutions can be divided into a high-pH/high-sulfide group (24-26) and a low-pH/low-sulfide group (20,22). In the former the pH change was very large (>1.40) and negative, while in the latter the pH change was quite small (approximately 0.25) and negative. Abundant, well-crystallized, pseudohexagonal, Cu-S minerals characterized the former group, whereas the latter showed only poorly-formed Cu-S phases.

Final Eh values for aerated, partially-deaerated and deaerated solutions ranged from 64.0 to 229.6 mV, 186 to 206 mV, and -350 to -386 mV, respectively. Sample 36 was -35 and the control sample was 84.0. For the aerated and partially-deaerated solutions an increase in the initial concentration of dissolved sulfide was generally correlated with a decrease in final Eh value. The deaerated solutions with very large, negative values for final Eh contained greater than 154 ppm of dissolved sulfide initially.

DISCUSSION

Many of the trends and correlations observed in the chemistry of the experimental solutions may be explained by examining the minerals that formed and analyzing the possible reactions by which they can form. Activity and Eh-pH (Pourbaix) diagrams are useful in such an analysis. These diagrams are also helpful for 1) summarizing aqueous solution/mineral relations, 2) recognizing disequilibrium, 3) suggesting when relative reaction rates, as well as, thermodynamic equilibrium, are determining the observed mineral assemblages, and 4) predicting the stable minerals that will form in various solutions. In the following sections the initial and final chemistry of the experimental solutions is discussed and evaluated in light of the mineralogy of the corrosion products that formed in those solutions. The results are plotted on various activity and Eh-pH diagrams in an attempt to explain the observed mineral assemblages and changes in solution chemistry. But first, the sulfur chemistry of the solutions must be elucidated.

Sulfur Chemistry of the Solutions

The dominant sulfur-bearing ions and molecules found in natural waters are SO_4^{2-}, HSO_4^{-}, S^{2-}, HS^{-}, H_2S and a variety of polysulfides (SS^{2-}, S_2S^{2-}, S_3S^{2-}, S_4S^{2-}, etc.). Eh and pH determine which sulfur species are present (Figure 13). [Thermodynamic data used in the construction of this and other diagrams are given in Table 11.] Figure 13 indicates that the dominant stable sulfur species in well-oxygenated seawater is SO_4^{2-}. HS^{-}, H_2S and polysulfides are the species most commonly found in reducing conditions. The pH values for which S^{2-} or HSO_4^{-} will be dominant species are considerably outside the range of average seawater and the experimental solutions prepared for this research.

Syrett et al.[1] and Giggenbach[17] have shown that the polysulfides SS^{2-}, S_2S^{2-}, S_3S^{2-} and S_4S^{2-} may exist in sulfide-polluted seawater, but that only S_3S^{2-} and S_4S^{2-} are present in significant quantities. Data presented by Syrett et al.[1] indicated that the equilibrium molar ratio of species at a pH of approximately 8.3 is $[HS^{-}] : [S_3S^{2-}] : [S_4S^{2-}] = 1 : 0.0263 : 0.126$. The presence of polysulfides in seawater increases corrosion rates of copper alloys [1], however, in the course of this experimental work the concentrations of polysulfides could not be determined. Therefore, only the four species SO_4^{2-}, H_2S, HS^{-} and S^{2-} are considered in this paper. Of these, only HS^{-} and SO_4^{2-} are important for the range of Eh and pH observed in this study.

The reduced sulfur added to the experimental solutions in the form of $Na_2S\ 9H_2O$ can be oxidized to SO_4^{2-} depending on the level of oxidizing agents available in the solutions. Avrahami and Golding[18] and Millero et al.[19] found that dissolved sulfide is oxidized rapidly in seawater. They determined values for the half-life of hydrogen sulfide (H_2S) in seawater of 20 minutes and 26 (+ 9) hours, respectively. Even assuming the longer half-life, any significant additions of sulfate to these solutions due to oxidation of sulfide would have occurred within the first week of the experiment. Calculations showed that the oxidation of sulfide in solution could make only an inconsequential addition to the sulfate content of the synthetic seawater solutions. Even assuming that all the dissolved oxygen in the solution was used to convert HS^- to sulfate, the maximum possible increase in sulfate concentration would be an insignificant 2.00×10^{-4} mol/l (<1%). Sulfate in these experimental solutions was not reduced because reduction of seawater sulfate requires bacterial catalysis [20], as it is a slow process even by geologic standards. Therefore, the dissolved sulfate concentrations in these solutions can be accurately represented by the dissolved sulfate concentration of the initial synthetic seawater solution.

The speciation of reduced sulfur was estimated using pH and the concentration of total dissolved sulfide (S_T) in each solution (Table 3). S_T is related to the concentration of the individual reduced sulfur species by the following equation:

$$S_T = HS^- + H_2S + S^{2-}. \qquad (1)$$

For this calculation the two dissociation constants chosen for H_2S were $pK_1 = 6.514$ ($K = 10^{-6.514}$) [21] and $pK_2 = 17.323$ ($K=10^{-17.323}$) [modified from Schoonen and Barnes [22]]. At the pH values encountered in these solutions ($7.84 < pH < 8.45$), it was determined that H_2S initially made up less than 5% of the reduced sulfur with S^{2-} contributing at most six orders of magnitude less than that. Only solutions 30 - 34 had detectable dissolved sulfide remaining at the end of the corrosion experiment. The pH values in these solutions had risen to 8.45 - 8.71, so, the concentration of H_2S was even less than initially and amounted to less than 2% of the reduced sulfur. The estimated concentration of S^{2-} was less than 7×10^{-12} M. HS^- is, therefore, the dominant reduced sulfur species considered in this paper.

Conditions of Mineral Formation

Figures 14 and 15 show the stability fields of the copper minerals most likely to occur in natural, sulfide-poor seawater (i.e., tenorite, brochantite, malachite, azurite, and paratacamite). A number of solution variables determine which of the common cupric minerals form. For this research products of the activities of the hydrogen, chloride, and sulfate ions are graphed versus the pressure of CO_2 gas. The dots show the composition of the aerated solutions that were very close in composition to natural seawater. The squares show the composition of the deaerated and partially-deaerated solutions. The latter solutions were bubbled with nitrogen gas to remove oxygen, which also removed most of the dissolved CO_2 gas. The CO_2 pressures of these latter solutions are estimates.

Figure 15 predicts that there is not enough sulfate in any of these solutions to stabilize brochantite with respect to tenorite and malachite. Figure 14 predicts that either malachite or paratacamite should form and both these minerals are, in fact, observed corroding copper, bronze or brass in seawater. Paratacamite was the phase observed in the most sulfide-poor (< 9 ppm) solutions of these experiments. The small amounts of Cl added as HCl to adjust initial pH values apparently stabilized paratacamite with respect to malachite in the aerated solutions.

Cuprite and aragonite also appeared on the samples corroded in the sulfide-poor, aerated solutions. Cuprite was observed beneath the paratacamite, and aragonite on top of the copper-chloride phase. The first corrosion product to form on the Cu-alloy was probably cuprite followed by the formation of paratacamite. A reaction such as the following could account for the formation of paratacamite in these solutions:

$$2Cu_2O_{(s)} + 2Cl^-_{(aq)} + 2H_2O_{(l)} + 2H^+_{(aq)} + O_{2(aq)} = Cu_4(OH)_6Cl_{2(s)}. \qquad (2)$$

The formation of paratacamite consumes H^+ ions causing an increase in pH. Just such an increase in pH was observed in solution 2 in which paratacamite was formed.

Due to an increase in pH precipitation of paratacamite via reaction (2) in some cases may have initiated the following reaction:

$$Ca^{2+}_{(aq)} + HCO_{3(aq)}^- = CaCO_{3(s)}(\text{aragonite}) + H^+_{(aq)} \qquad (3)$$

This may explain the occurrence of aragonite on sample 4. The formation of aragonite crystals releases H^+ ions which possibly explains the small pH decrease observed on sample 4. Precipitation of aragonite, therefore, tends to counteract the effect of paratacamite precipitation. When reactions (2) and (3) both occur pH could remain virtually unchanged. On sample B aragonite and paratacamite were observed and the initial and final pH values in the solution were the same (8.40). The corrosion product formed in the partially deaerated solution with 1 ppm initial dissolved sulfide (sample # 20) was also dominated by paratacamite. The pH of this solution decreased slightly during the course of the experiment. Hydrolysis of cupric ion may have been responsible for this.

Reactions occurring in solutions with sufficient dissolved oxygen can form highly acidic sulfur species, such as sulfurous acid (H_2SO_3). Syrett [9] found that such sulfide oxidation reactions are accompanied by a pH decrease. Some aerated (6, 8, 16, 10, 12, 14) and partially deaerated (22, 24, 26, 36) samples experienced a pH decrease during production of the sulfide corrosion product. This may have been due to H_2SO_3 formation in solutions with sufficient oxygen to oxidize substantial amounts of sulfide. With so many complex reactions possible it is difficult to predict the differences in solution conditions that may favor one over the other.

The corrosion products formed in solutions where significant variations in oxidation potential were observed are best evaluated using plots such as Figures 16, 17, and 18. These Eh-pH diagrams show the stability fields of some of the common copper corrosion products, and the initial and final solution compositions. To construct them the reactions occurring at the phase boundaries were written involving the dominant sulfur species for those Eh-pH conditions. On Figure 16 the solid and dashed boundaries were drawn assuming concentrations of the aqueous sulfur species to be 10^{-2} and

10^{-4} mol/L, respectively. This is the approximate range of dissolved sulfur activities observed during this research. Figure 16 indicates how the sizes of the various stability fields change as the activities of dissolved sulfur species change. For simplicity, Figures 17 and 18 are drawn for a single activity of dissolved sulfur species of 10^{-3}, which is in the middle of the range observed. Also, the initial and final solutions compositions are plotted separately and their oxygen contents are indicated.

The stability fields for digenite and djurleite were not included on these diagrams due to the lack of accurate thermodynamic data for those minerals. Djurleite and digenite have copper to sulfur ratios intermediate to those of covellite and chalcocite and could be expected to form under conditions between those which favor formation of covellite and chalcocite. When accurate data become available, the fields of djurleite and digenite may appear as very narrow bands wrapped around the covellite field.

The initial pH and estimated Eh values of the experimental solutions are plotted on Figure 17. Solutions 2, 4, and 6, all plot in, or on the boundary of, the cuprite field. No significant Cu-S phases were observed on these samples. Solution 20, which also did not develop a Cu-S phase, did not initially plot up with the other oxidized solutions, but instead plotted in the cuprite field. Solutions 8, 16, 22, and 24 plotted near the native copper/Cu_2S boundary and all samples except 24 developed poorly-formed, pseudohexagonal Cu-S crystals, which are probably chalcocite. Sample 24 developed well-formed Cu-S crystals.

The remaining solutions initially plotted well within the stability fields of the Cu-S phases. Cu-Ni wafers corroded in these solutions all show well-formed, Cu-S crystals suggesting that they formed under conditions more favorable for the precipitation of the reduced copper-sulfide minerals. Minerals identified by EDX and SEM analysis are generally those predicted by the Eh-pH diagram.

The three deaerated samples: 30, 32, and 34; initially contained 154, 192 and 248 ppm of dissolved sulfide, respectively. They plot close together in the chalcocite or covellite stability fields on Figures 17 and 18. The dominant reaction taking place in these solutions may have been [6,9] :

$$2Cu^{o}{}_{(s)} + HS^{-}{}_{(aq)} + H^{+}{}_{(aq)} + 1/2O_{2(aq)} = Cu_2S_{(s)} + H_2O_{(l)}. \qquad (4)$$

Once the solution became completely depleted in dissolved oxygen the following reaction [described by Syrett [9]] may have been responsible for the attack on the wafer:

$$2Cu^{o}{}_{(s)} + HS^{-}{}_{(aq)} + H^{+}{}_{(aq)} = Cu_2S_{(s)} + H_{2(g)}. \qquad (5)$$

Reactions such as the two above would cause an increase in pH by consuming hydrogen ion. Such an increase was observed in solutions 30, 32 and 34. These are the only three solutions which remained within the stability fields of the copper sulfide minerals for the entire 4 months of the corrosion experiments. At the end of the experiment all other solutions plotted in the cuprite or paratacamite fields, however, well-formed copper-sulfide phases persisted in many of these solutions.

These experiments are parallel to the microbiological alteration studies of Baas-Becking and Moore [13], McNeil et al.[10] and others, and it is interesting to consider differences and similarities. The water chemistry in these experiments remains near neutral. This is normal for a bulk seawater experiment, but may represent conditions quite different from those near an anodic site under a biofilm. The conditions are also different from those observed by McNeil et al.[10] during experiments on marsh and lake waters. In experiments with aerated water, the Eh appears to drop at first and then to remain relatively oxidizing. This is very different from measurements under biofilms (R. Newman, private communication, 1991) which indicate very reducing environments. In biofilms in natural environments, therefore, there is a continuous source of sulfide ions and a local reducing environment. This may explain why in estuarine environments blue-remaining covellite is found (J. Craig, private communication, 1991), while laboratory experiments do not synthesize it except under very special conditions not representative of the biosphere.[23]

On Figure 13 the initial and final solution compositions are plotted on an Eh-pH diagram showing the stability fields of the dominant species of dissolved sulfur. Initially, only aerated samples 12 and 14, and partially deaerated or aerated samples 30-36 plotted in the HS^- stability field. In all other samples, SO_4^{2-} was the stable form of aqueous sulfur. In these latter samples oxidation of sulfide would have begun immediately upon addition. Even assuming the longer half-life of 26 hours for H_2S [19], the sulfide level in the most concentrated of the solutions would have been reduced to < 2 ppm in the first week. Although such low sulfide levels are not conducive to Cu-S mineral formation, copper sulfide minerals were observed in most of these solutions. This suggests that the reduced sulfur was scavenged rapidly by copper, possibly forming an amorphous or cryptocrystalline Cu-S phase which later crystallized to chalcocite, djurleite, digenite, or possibly covellite.

These observations suggest a model for this abiotic sulfiding corrosion. They are consistent with the hypothesis that most of the sulfide reacts with water and copper almost immediately (probably within a week). The result of the reaction with copper may be an amorphous or cryptocrystalline sulfide. Its formation may parallel that of the amorphous sulfide conjectured to exist as a precursor to mackinawite (FeS_{1-x}) in sulfiding corrosion of iron. [24] This compound then reacts to produce the sulfide minerals generally observed in copper-sulfiding corrosion. It is significant to note that the sulfide minerals persist, and perhaps even alter to other sulfide minerals, in such an oxidizing environment. This is in contrast to the observations of Olowe et al.[25] on iron. They found that if local conditions became oxidizing the low iron sulfides, such as mackinawite, altered to green rust 2 - a sulfate compound. This difference probably reflects the greater stability of low copper sulfides, such as chalcocite, with respect to the oxidized copper minerals.

Despite the frequent observation of sulfide minerals in corrosion, and the fact that millerite (NiS), at least, can be produced by SRB, no observation of nickel sulfides in copper-nickel alloy corrosion products has ever been made. This may be explained by the model put forward here. Dissolved divalent nickel ions exchange waters of hydration with the groundwater much more slowly than dissolved divalent copper ions.[26] This fundamental difference in reactivity makes nickel oxide dissolve much more slowly than copper oxide. This difference is likely to extend to other minerals.[26] This suggests that the copper binds with all available sulfide ions before the nickel can.

Potential for Corrosion Protection

The development of a corrosion product film that may afford the alloy some protection from further corrosion depends on the chemistry of the solution, the mineralogy of the corrosion product, and the mineral assemblage. As postulated by many researchers, cuprite may be somewhat protective if it can be preserved, however, it is readily converted to other minerals. This research provided evidence for this as cuprite was only rarely observed. When cuprite occurs as part of a porous, heterogeneous Cu-O-Ni-Fe-S layer it is even less likely to provide any protection. The paratacamite films observed showed poor-to-good adherence, but paratacamite is often associated with pitting. The thin, cracked underlayer of Cu-S-Ni-Fe appears to offer little prospect of corrosion protection, as it shows very poor adherence and minimal internal cohesion. These heterogeneous films have the additional disadvantage that layers made of interpenetrating crystals of differing morphologies may be more porous to corrosive ions.[3] These nonprotective, corrosion films formed in aerated solutions containing less than or equal to 8 ppm dissolved sulfide, and in partially deaerated solutions having less than 8 ppm dissolved sulfide.

The other corrosion films were dominated by relatively pure Cu-S minerals occurring either as well-developed crystals or lepispherical masses of poorly-formed crystals. These films ranged from being nonadherent to showing good adherence. In the aerated solutions only the films formed under conditions of high, initial sulfide (samples 12 and 14) showed good adherence. Electron microprobe analysis of sample 14 indicated only chalcocite, which is described as non-protective. These samples were also composed of both the hexagonal and serrated Cu-S phases which would tend to enhance corrosion rates. Only the most sulfide-rich, partially deaerated solution produced a homogeneous, adherent coating composed dominantly of one type of Cu-S crystal -- the pseudo-hexagonal variety (probably chalcocite with small amounts of a copper-poor sulfide). Corrosion films formed in deaerated solutions all exhibited good adherence and were dominated by Cu-S crystals showing a single morphology -- two were dominated by the hexagonal crystals (30 and 34) and one by the serrated crystals (32). As discussed previously these three samples are the most likely to contain the potentially protective mineral djurleite.

In summary, adherent films appear to form only in deaerated solutions or in solutions with very low or very high initial sulfide levels (i.e., S^{2-} >200 ppm or < 9 ppm). Also, solutions plotting initially in the stability field of HS^- produced Cu-S films with good adherence. Few of these films, however, are likely to protect Cu-alloys from further corrosion. Only the solutions with initial dissolved sulfide concentrations greater than 150 ppm produced both adherent, homogeneous and potentially-protective films. Most of these films, however, are probably dominated by chalcocite which is non-protective.

If djurleite does form a coating which enhances the corrosion resistance of copper alloys [11], it will most likely form under the same conditions as those that produced the homogeneous adherent films in deaerated, high-sulfide solutions (30-34). Figures 13, 16, and 17 show the initial and final Eh-pH conditions under which these films formed. Note that only these three solution compositions fall within the stability fields of the copper sulfide minerals throughout the entire experiment. Djurleite is in an intermediate sulfidation state between that of covellite and chalcocite, therefore, it would be expected to form under conditions such as those indicated for these solutions. Microprobe analyses of samples 30 and 32 suggest the presence of a copper-poor sulfide which may be djurleite.

CONCLUSIONS

Chalcocite and possibly djurleite, digenite, and small amounts of covellite, were formed abiotically in synthetic seawater solutions with varying Eh, pH and concentrations of dissolved oxygen and sulfide. Formation of these well-crystallized Cu-S minerals may have been preceded by growth of an amorphous or cryptocrystalline Cu-S phase. This postulated, precursor phase probably began forming as soon as the Cu-Ni wafer was immersed and may have been nearly completed within the first week of the experiment. In the case of microbiologically-influenced corrosion, SRB appear to maintain a reducing, high-sulfide, possibly low-pH environment near the metal surface. Conditions in these abiotic experiments, however, became quite oxidizing and sulfide-poor in the latter stages of the corrosion process. Overall initial pH seems to correlate less significantly with other solution parameters and corrosion-product mineralogy than any other chemical characteristic of the solutions. Dissolved sulfide and oxygen concentrations appear to influence the course of the corrosion process more significantly. If djurleite can provide corrosion protection, deaerated, sulfide-rich solutions seem to offer the best prospect for coating Cu-alloys with such protective Cu-S films.

ACKNOWLEDGEMENTS

I gratefully acknowledge the efforts of Dr. Peter Zhdan and Dr. James Castle at the University of Surrey, who provided the XPS analysis. Todd Solberg and Dr. James Craig of the Virginia Polytechnic Institute provided the use of the electron microprobe and helped with sample preparation and collection of the data. This work was supported by the Office of Naval Research, Program Element 61153N, through the NOARL Defense Research Sciences Program. NOARL Contribution Number 333:022:92.

REFERENCES

1. B.C. Syrett, D.D. MacDonald, S.S. Wing, Corrosion, 35,(1979):p. 409.
2. R.B. Niederberger, J.D. Gudas, G.J. Danek,CORROSION/76,paper no. 76, (Houston, TX: NACE, 1976).
3. B.C. Syrett, Corrosion, 21,(1981): p. 187.
4. B.C. Eiselstein, S.S.Wing, R. D. Caligiuri, Corrosion Science, 23,(1983):p. 223.
5. E.D.Mor, A. M. Beccaria, British Corrosion Journal,10,(1975):p. 33.
6. N. Mukhopadhyay,S. Baskaran, Corrosion, 42,(1986):p. 113.
7. D.D.MacDonald, B.C.Syrett, S. S. Wing, Corrosion, 35, (1979):p. 367.
8. R.F. North,M. J. Pryor, Corrosion Science, 10, (1970):p. 297.
9. B.C. Syrett, Corrosion, 33, (1977):p. 257.
10. M.B. McNeil, J.M. Jones, B.T. Little, Corrosion, 47, (1991):p. 674.
11. N.A. North,I. D. Macleod, Corrosion of Metals IN: Conservation of Marine Archaeological Objects, (C. Pearson, ed.) (London, Butterworths, 1987), p. 81.
12. E. Roseboom, Economic Geology, 61,(1966):p. 641.
13. L. Bass-Becking,D. Moore, Economic Geology, 56,(1961):p. 259.
14. P.A. Schweitzer, What Every Engineer Should Know About Corrosion (New York: M. Decker, 1987), p. 21.
15. J.Lyman,R.H.Fleming, Journal of Marine Research, 3,(1940):p. 134.
16. D. Kester, E.W. Duedall, D.N. Connors, R. M. Pytkowicz,Limnology and Oceanography, 12,(1967):p. 176-178.
17. W.F. Giggenbach, Inorganic Chemistry, 11,(1972):p. 1201.
18. M. Avrahami,R.M. Golding, Journal Chemical Society, A,(1968):p.647
19. F. Millero, S. Hubinger, M. Fernandez,S. Garnett,Environmental Science & Technology, 21,(1987):p. 439.
20. J. Boulegue, Geochimica et Cosmochimica Acta, 42,(1978):p. 1439.
21. F. Millero, T. Plese,M. Fernandez, Introduction to Marine Chemistry, 33,(1988):p. 269.
22. M.A. Schoonen, H. L. Barnes, Geochimica et Cosmochimica Acta,52, (1987):p. 649.
23. D.T. Rickard, Stockholm Contributions Geology, 23, (1971):p.1.
24. J. Morse, F. Millero, J. Cornwell, D. Rickard, Earth Science Reviews,24,(1987):p.1.
25. A. Olowe, P. Bauer, J. Genin,J. Guezennec, Corrosion, 45,(1989):p. 229.
26. W. Casey, Journal of Colloid and Interface Science, 146, (1991): p.586.
27. T.L. Woods,R.M. Garrels, Economic Geology, 81,(1986):p.1989.

Table 1

Chemical formulae and crystallographic characteristics of selected copper minerals.

Mineral	Formula	Crystal habit	Crystal system
Anilite	Cu_7S_5	Probably pseudo-hexagonal	ortho
Antlerite	$Cu_3(OH)_4SO_4$	Nearly equant	ortho
Aragonite	$CaCO_3$	Acicular prisms	ortho
Azurite	$Cu_3(OH)_2(CO_3)_2$	Tabular or prismatic globular radiated	mon
Blaubleibender (Blue remaining covellite)	$Cu_{1+X}S$	Hexagonal tabular crystals or massive	hex
Brochantite	$Cu_4(OH)_6SO_4$	Acicular, tabular	mon
Chalcocite	Cu_2S	Pseudo-hexagonal tabular crystals usually massive	mon
Covellite	CuS	Hexagonal tabular crystals or massive	hex
Cuprite	Cu_2O	Cubes and octahedrons	iso
Digenite	$Cu_{1.8}S$	Pseudo-hexagonal crystals	iso
Djurleite	$Cu_{1.97}S$	Rarely as pseudo-hexagonal, tabular crystals. Usually massive	mon
Malachite	$Cu_2(OH)_2CO_3$	Prismatic, acicular botryoidal	mon
Paratacamite	$Cu_4(OH)_6Cl_2$	Rhombohedral dipyramidal	hex

Notes: Key to abbreviations:
mon - monoclinic
ortho - orthorhombic
tri - triclinic
iso - isometric
hex - hexagonal

Table 2

Comparison of the composition of natural and synthetic seawaters (from Kester et al., 1967)

Ion	Artificial seawater (gms/kg of seawater)	Natural seawater (gms/kg of seawater)
Cl^-	19.353	19.353
Na^+	10.764	10.760
SO_4^{2-}	2.701	2.712
Mg^{2+}	1.297	1.294
Ca^{2+}	0.406	0.413
K^+	0.387	0.387
HCO_3^-	0.142	0.142
Br^-	0.066	0.067
Sr^{2+}	0.000	0.008
H_3BO_3	0.026	0.026
F^-	0.001	0.001

Table 3

Summary of chemical data for experimental solutions.

Specimen Number	Oxygen Mg/L Initial	** Eh Initial mV	Eh Final mV	Approximate Δ Eh	Initial pH	Final pH	Δ pH	Initial Sulfide ppm	Final Sulfide ppm
1,2	7.00	40	224	180	8.14	8.18	0.04	1	BDL
3,4	7.00	30	216	190	8.45	8.10	-0.35	8	BDL
5,6	7.00	- 20	214	230	8.14	7.49	-0.65	40	BDL
7,8	7.00	-140	230	370	8.42	7.47	-0.95	115	BDL
16,17	7.00	-200	228	430	8.15	6.70	-1.45	154	BDL
10,11	7.00	-260	150	410	8.40	8.06	-0.34	192	BDL
12,13	7.00	-360	100	460	8.35	8.24	-0.11	256	BDL
14,15	7.00	-410	83	500	8.39	7.89	-0.50	289	BDL
20,21	0.10	-130	206	340	8.10	7.86	-0.24	1	BDL
22,23	0.10	-140	204	350	7.84	7.58	-0.26	8	BDL
24,25	0.10	-200	193	390	8.24	6.82	-1.42	58	BDL
26,27	0.10	-270	186	460	8.25	6.80	-1.45	115	BDL
30,31	0.02	-360	-361	0	8.36	8.71	0.35	154	58
32,33	0.02	-410	-357	50	8.07	8.65	0.58	192	96
34,35	0.02	-470	-386	90	8.29	8.45	0.16	248	160
36,37	0.10	-480	-35	510	8.42	8.41	-0.01	289	BDL
A	0.10	-130	84	214	8.40	8.60	0.20	0	0
B	7.00	42	64	22	8.40	8.40	0.00	0	0

BDL = Below detection limit: detection limit for sulfide electrode is 10^{-7}M, S^{2-}

**estimated from method described in text, subject to an error of at least 50 mV

Table 4A
Macroscopic Characteristics of Wafers

Specimen Number	Description
2	Thin, reddish-brown coating, poorly adherent.
4	Thick, adherent, green coating with abundant, acicular, white crystals.
6	Thin, poorly adherent, black coating with black tarnish where coating washed away.
8	Thick, poorly adherent, black coating. Washed off on edges exposing tarnished wafer.
10	Thick, non-adherent, black coating.
12	Thick, brown, adherent coating.
14	Thick, brown, adherent coating.
16	Thick, non-adherent, dark gray-to-black coating.
20	Thin, adherent, tarnished, brown corrosion film with patches of blue and green.
22	Thick, adherent, black coating.
24	Thick, non-adherent, dark-gray coating.
26	Thick, non-adherent, black coating.
30	Thick, brownish-gray, adherent coating.
32	Thick, brown, adherent coating in center with green and yellow coating at edges.
34	Thick, black, adherent coating covered with white, acicular crystals.
36	Thick, brown, adherent coating.

Microscopic Characteristics of Wafers

Specimen Number	Description
2	In areas where reddish-brown product washed away, a thin film containing numerous cracks and cubes of Cu_2O was visible. Brownish-red coating appeared as lepispherical masses of paratacamite crystals.
4	Top layer consisted of packets of acicular $CaCO_3$ crystals. Lepispherical masses of paratacamite were also abundant in this layer. The bottom layer consisted of a thin, black, cracked film containing Cu_2O crystals.
6	Rare $CaCO_3$ in top layer. Poorly-formed, pseudo-hexagonal Cu_2S crystals doped with Fe & Ni dominate top.
8	Upper surface of corrosion film consists of poorly-formed, pseudo-hexagonal Cu_2S & rare $CaCO_3$. A thin, apparently porous, layer of platy Cu-S minerals underlies the upper surface.
10	Abundant Cu_2O cubes and pseudo-hexagonal Cu_2S crystals Elongate, platy Cu_2S crystals with serrated edges were intermixed with the Cu_2O and pseudo-hexagonal crystals
12	Upper layer composed of pseudo-hexagonal Cu_2S and elongate, platy Cu_2S with serrated edges. Packets of $CaCO_3$ crystals surrounded by Fe-rich nodules were also abundant in upper layer.
14	Corrosion film composed predominantly of $CaCO_3$, underlain by elongate Cu_2S with serrated edges.
16	Upper layer is predominantly intergrown, poorly-formed, pseudo-hexagonal Cu_2S crystals. Cubic Cu_2O was exposed in areas where Cu_2S coating was removed.
20	Coating composed of poorly-formed paratacamite crystals
22	Coating composed of poorly-formed pseudo-hexagonal Cu_2S
24	Coating composed of tabular and dipyramidal, pseudo-hexagonal Cu_2S crystals.
26	Upper layer dominated by packets of $CaCO_3$ crystals. The underlying layer consists of tabular and dipyramidal, pseudo-hexagonal Cu_2S. Elongate, platy Cu_2S crystals with serrated edges are intermixed.
30	Upper layer dominated by tabular, pseudo-hexagonal Cu_2S intermixed with elongate, serrated Cu_2S phase.
32	Coating dominated by elongate, serrated Cu_2S crystals. Intermixed within the upper layer are tabular pseudo-hexagonal Cu_2S crystals.
34	Coating dominated by tabular, pseudo-hexagonal Cu_2S intermixed with elongate, serrated phase. Overlain by $CaCO_3$ crystals.
36	Coating dominated by tabular, pseudo-hexagonal Cu_2S intermixed with $CaCO_3$ crystals. Elongate, serrated Cu_2S phase was present, but rare.

Table 5
XPS and XAES data for deaerated samples

Sample	S2p B.E. (eV) (1)	S2p B.E. (eV) (2)	S KLL K.E. (eV) (1)	S KLL K.E. (eV) (2)	$Ni2p_{3/2}$ B.E. (eV)	$Cu2p_{3/2}$ B.E. (eV)	Cu L_3VV K.E. (eV)	Cu AP (eV)	S AP (eV)
CNB	—	—	—	—	852.4	932.4	918.6	1851.0	—
20	162.2	169.2	2115.2	2107.8	858.4	932.8	918.6	1849.2	2277.4
	162.4	—	2114.8	—	856.2	932.4	916.4	1848.8	2277.2
22	162.4	—	2115.2	—	859.2	932.4	918.4	1848.8	2277.6
24	162.2	—	2115.4	—	858.4	932.4	916.4	1848.8	2277.6
	162.6	—	2115.2	—	856.6	932.4	916.4	1848.8	2277.8
26	161.8	169.0	2118.2	2107.6	856.0	932.2	917.2	1849.4	2278.0
	162.6	169.4	2114.8	2107.0	856.4	932.4	918.4	1848.8	2277.4
30	162.2	—	2115.2	—	—	934.2	916.2	1850.4	2277.4
	—	—	—	—	—	934.8	916.2	1850.8	—
32	162.2	—	2115.6	—	857.0	932.4	916.4	1848.8	2277.8
	162.2	—	2115.7	—	862.4	932.4	918.4	1848.8	2277.9
34	161.6	—	2118.1	—	856.4	932.0	917.0	1849.0	2277.7
	—	—	—	—	—	932.4	918.4	1848.8	—
36	162.6	—	2115.4	—	856.2	932.5	918.2	1848.7	2278.0
	—	—	—	—	857.4	933.2	917.1	1850.4	—

CNB = Standard sample

Table 6
XPS and XAES data for aerated samples

Sample	01s B.E. (eV)	S2p B.E. (eV) (1)	S2p B.E. (eV) (2)	S KLL K.E. (eV) (1)	S KLL K.E. (eV) (2)	$Ni2p_{3/2}$ B.E. (eV)	$Cu2p_{3/2}$ B.E. (eV)	Cu L_3VV K.E. (eV)	Cu AP (eV)	S AP (eV)
2	531.8	161.7	168.4	2115.8	—	856.0	932.8	916.6	1849.2	2277.3
4	531.6	—	168.9	—	2108.0	856.0	933.4	915.6	1849.0	2276.9
	531.6	162.1	168.8	2115.4	2107.8	856.0	932.4	916.4	1848.8	2277.5
6	531.6	162.7	168.8	2113.8	2107.4	858.2	932.4	916.4	1848.8	2276.5
	532.0	162.6	—	2115.4	—	856.4	932.4	916.6	1848.8	2278.0
8	531.8	162.6	168.8	2115.2	2107.5	856.2	932.4	916.6	1849.0	2277.8
	531.8	162.6	168.8	2115.0	—	856.2	932.4	916.4	1848.8	2277.8
16	531.8	162.2	169.2	2115.6	2107.2	856.2	932.4	916.8	1849.2	2277.8
	531.8	162.0	—	2115.6	—	856.2	932.4	916.6	1849.0	2277.6
10	531.8	162.6	—	2115.2	—	858.8	933.2	917.4	1850.6	2277.8
	531.8	163.0	—	2114.5	—	856.4	932.4	917.6	1850.0	2277.5
12	530.8	162.0	—	2115.0	—	—	932.8	916.6	1851.2	2278.0
	530.8	162.4	—	—	—	855.8	932.4	916.4	1848.8	—
14	531.8	162.4	—	2115.6	—	856.6	932.8	916.2	1849.0	2278.0
	531.8	162.4	—	2116.0	—	855.6	932.8	916.6	1849.2	2278.4

Table 7
Surface compositions of deaerated samples (in atomic %)

Sample	Cu	Ni	S	Cl	Ca	N	O	Mg	Na
20	23.5	3.2	1.2	0.8	3.1	3.7	60.2	1.0	3.3
	28.6	7.3	1.3	5.0	—	—	57.0	0.8	—
22	26.4	15.0	—	1.3	—	—	57.3	—	—
	38.8	8.3	0.7	1.1	0.8	0.8	47.3	2.2	—
24	33.0	11.9	—	2.5	0.5	1.2	48.5	1.4	—
	47.2	7.8	—	1.0	—	3.0	41.0	—	—
26	13.8	13.1	4.1	2.7	6.3	2.1	57.0	—	—
	30.2	13.0	—	3.4	—	2.2	50.5	0.7	1.0
30	26.0	1.0	—	—	—	1.0	71.5	—	0.5
	25.6	1.0	—	—	—	—	73.2	—	0.2
32	28.8	2.5	2.2	0.8	0.9	7.8	54.8	1.2	1.2
	49.8	0.9	—	—	0.9	0.8	45.2	0.5	0.8
34	27.3	5.0	3.0	—	0.5	4.1	57.5	1.3	1.3
	19.2	0.3	—	—	11.1	2.9	63.1	—	3.3
36	32.5	7.5	—	—	6.3	1.2	53.3	1.3	3.5
	12.9	0.4	—	—	9.7	0.8	75.0	1.2	0.8

Table 8
Surface compositions of aerated samples (in atomic %)

Sample	Cu	Ni	S	Cl	Ca	N	O
2	13.0	4.0	3.0	4.5	7.5	3.0	65
4	4.2	2.0	—	2.1	15.8	2.9	73
	21.8	7.4	4.1	0.3	0.6	1.0	65
6	24.0	11.8	—	3.4	—	2.0	58.5
	34.0	10.2	—	3.2	—	—	52.4
8	18.2	12.2	4.4	—	0.2	1.5	63.5
	41.4	7.4	1.8	—	—	—	49.4
16	24.3	7.5	—	—	—	—	68.2
	31.5	7.0	3.8	—	—	—	57.8
10	23.0	6.0	—	—	1.5	—	69.5
	47.9	11.2	3.5	—	—	2.4	34.9
12	43.7	—	6.1	—	—	—	50.1
	35.6	11.3	—	—	—	—	53.0
14	32.6	2.6	—	—	—	—	53.3
	19.4	3.4	—	—	9.7	—	65.5

Table 9

A. Electron microprobe analyses of Cu-S minerals

Sample Number	Weight percent Cu	Ni	Fe	Mn	S	Cl	Total
14-A	79.392	0.301	0.000	0.000	20.196	0.015	99.90
14-B	77.808	2.019	0.215	0.042	19.887	0.103	100.07
14-C	78.526	0.271	0.095	0.000	19.821	0.028	98.74
30-A	77.619	0.417	0.038	0.029	20.760	0.000	98.86
30-B	79.945	0.120	0.000	0.001	20.437	0.043	100.55
30-C	78.913	0.118	0.000	0.000	20.649	0.028	99.71
30-D	75.581	4.611	0.622	0.083	20.652	0.117	101.67
30-E	79.683	0.426	0.085	0.000	19.821	0.081	100.10
30-F	77.815	0.660	0.166	0.024	19.923	0.003	98.59
32-A	78.728	0.193	0.024	0.029	19.056	0.000	98.04
32-B	79.386	0.504	0.180	0.000	19.809	0.028	99.91
32-C	80.142	0.053	0.047	0.001	20.576	0.003	100.82
32-D	79.457	0.178	0.053	0.000	20.008	0.005	99.70

B. Analysis recalculated on the basis of 1 S

Sample Number	Cu	Ni	Fe	Mn	Sum of Cations
14-A	1.984	0.008	0.000	0.000	1.992
14-B	1.974	0.055	0.006	0.001	2.036
14-C	2.000	0.007	0.003	0.000	2.010
30-A	1.887	0.011	0.001	0.001	1.900
30-B	1.974	0.003	0.000	0.000	1.977
30-C	1.928	0.003	0.000	0.000	1.931
30-D	1.847	0.122	0.017	0.002	1.988
30-E	2.029	0.012	0.002	0.000	2.043
30-F	1.971	0.018	0.005	0.001	2.000
32-A	2.080	0.006	0.001	0.000	2.087
32-B	2.020	0.014	0.005	0.000	2.039
32-C	1.965	0.001	0.001	0.000	1.967
32-D	2.004	0.005	0.002	0.002	2.013

Table 11
Thermodynamic data used in calculations of Eh-pH diagrams and activity diagrams.

Phase	Name	G_f kj/mol
Cu^0	native copper	0
Cu_2O	cuprite	-146.0
CuO	tenorite	-125.9
CuS	covellite	- 53.6
Cu_2S	chalcocite	- 86.2
H_2O	water	-237.1
S^{2-}	sulfide	+ 85.8
HS^-	bisulfide	+ 12.1
H_2S	hydrogen sulfide	- 27.8
SO_4^{2-}	sulfate	-744.5
H^+		0

1 Compiled by Woods and Garrels (1986)

Table 10

A. Electron Microprobe Analyses of Ni-rich Cu-S phases

Sample Number	Weight Percent Cu	Ni	Fe	Mn	S	Cl	Total
14-D	42.532	27.245	0.328	0.018	20.463	0.435	91.02
14-E	33.123	31.181	0.776	0.116	16.545	0.468	82.21
30-G	57.202	16.938	0.574	0.067	20.656	0.252	95.69
30-H	62.587	14.536	0.910	0.061	19.801	0.937	98.83
32-E	70.056	8.016	0.474	0.024	20.215	0.215	99.00
32-F	60.849	16.157	2.227	0.292	9.052	0.357	88.94
32-G	47.947	19.777	2.382	0.337	17.497	0.263	88.20

B. Mol fraction of the elements

Sample Number	Cu	Ni	Fe	Mn	S	Cl
14-D	0.374	0.259	0.003	0.000	0.356	0.007
14-E	0.326	0.332	0.009	0.001	0.323	0.008
30-G	0.486	0.156	0.006	0.001	0.348	0.004
30-H	0.520	0.131	0.009	0.001	0.326	0.014
32-E	0.585	0.072	0.004	0.002	0.334	0.003
32-F	0.610	0.175	0.025	0.003	0.180	0.006
32-G	0.446	0.199	0.025	0.004	0.322	0.004

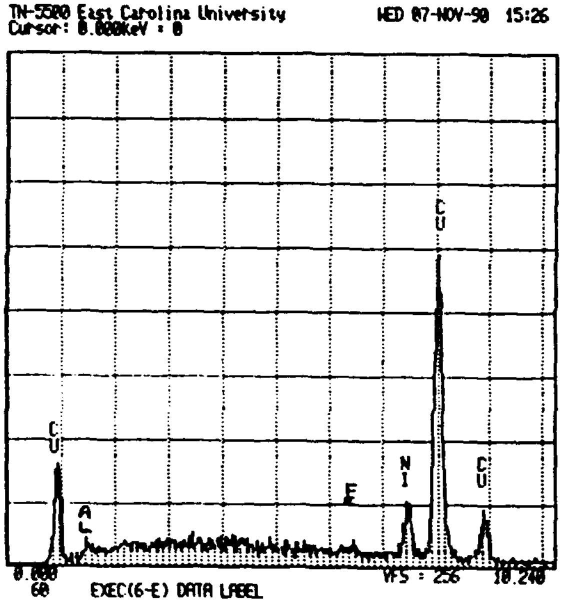

FIGURE 1 - Energy dispersive X-ray analysis of 90Cu-10Ni specimens prior to being placed in experimental solutions.

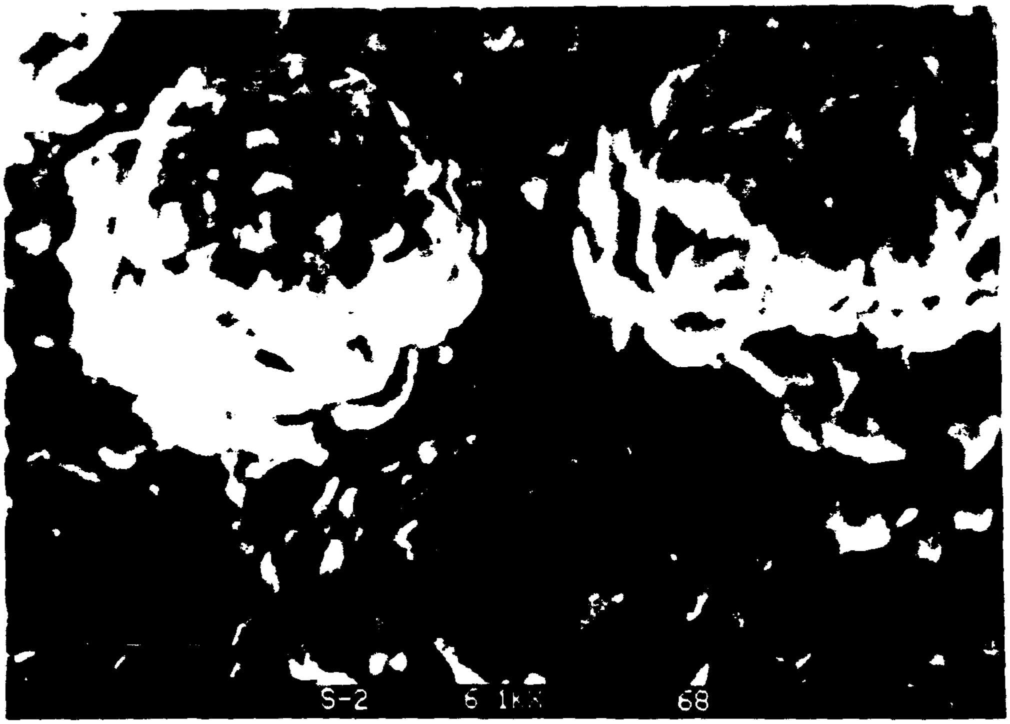

(A) magnification = 6,100X

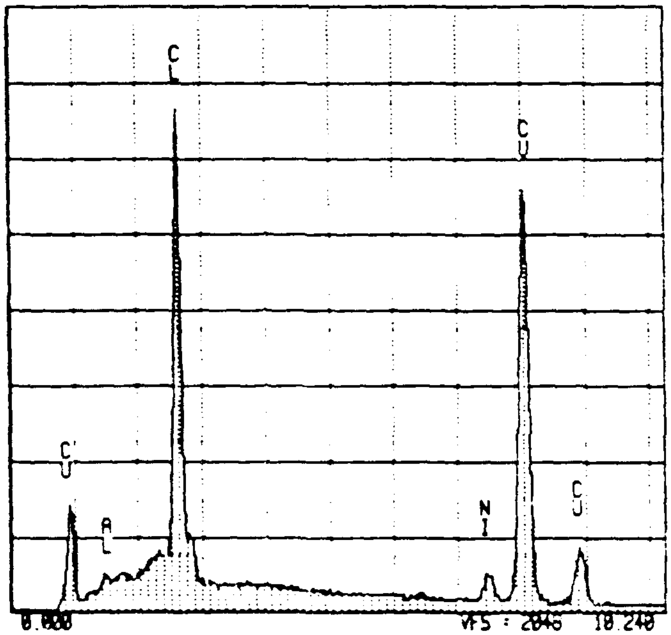

(B)

Figure 2. (A) SEM photomicrograph and (B) EDX analysis-lepispherical masses-paratacamite crystals.

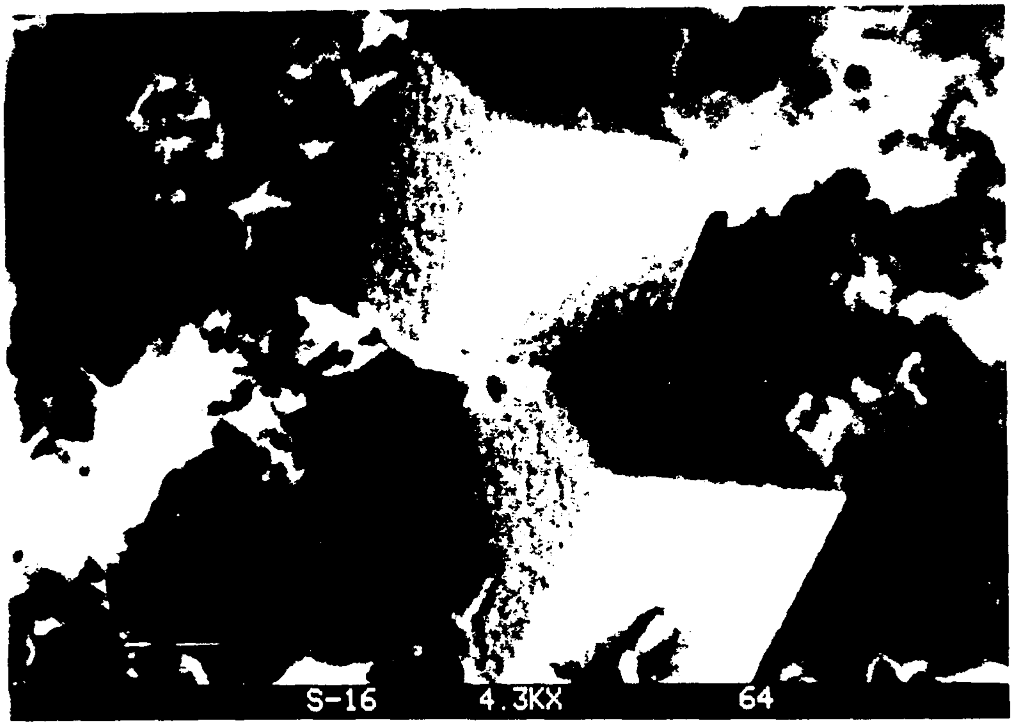

(A) magnification = 4300X

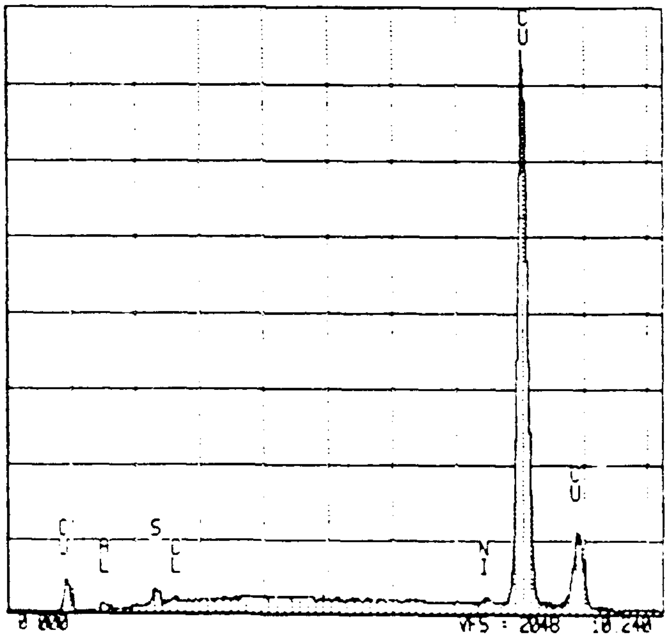

Figure [illegible]. (A)SEM photomicrograph and (B)EDX analysis of cubic cuprite crystals.

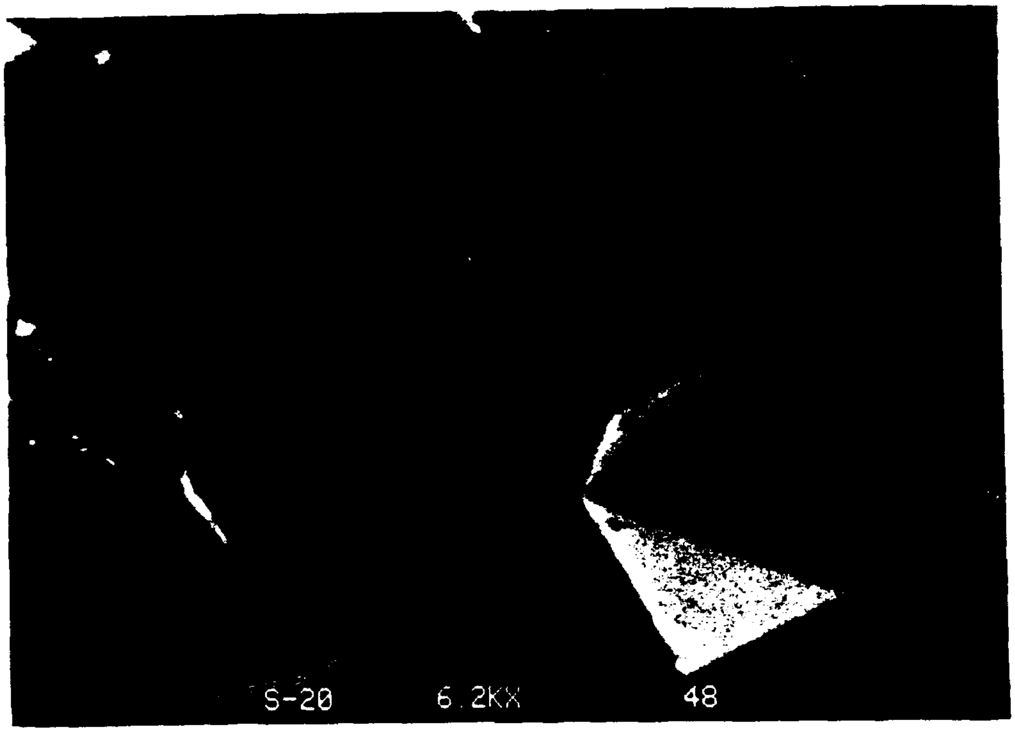

(A)magnification = 1250X

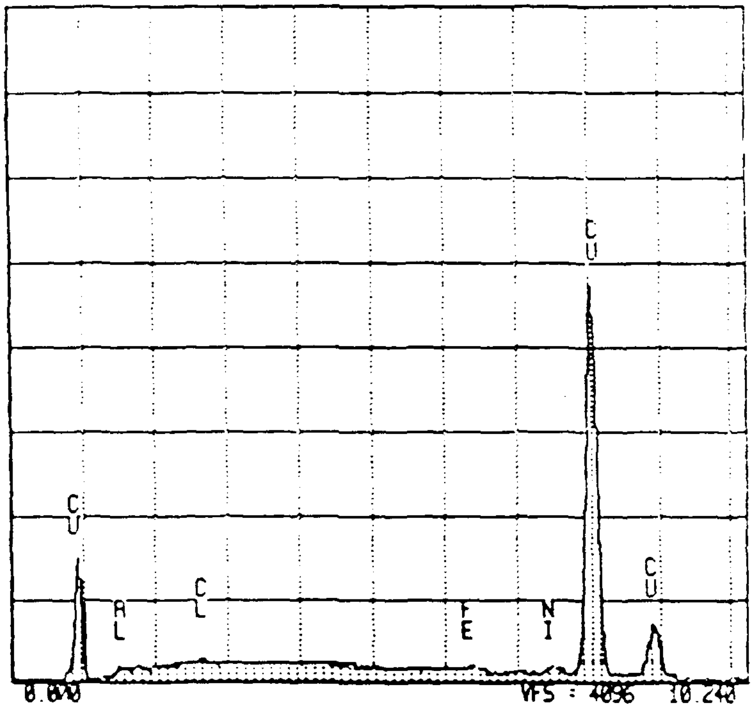

(B)

Figure 4 : (A) SEM photomicrograph and (B) EDX analysis of octahedral cuprite crystals.

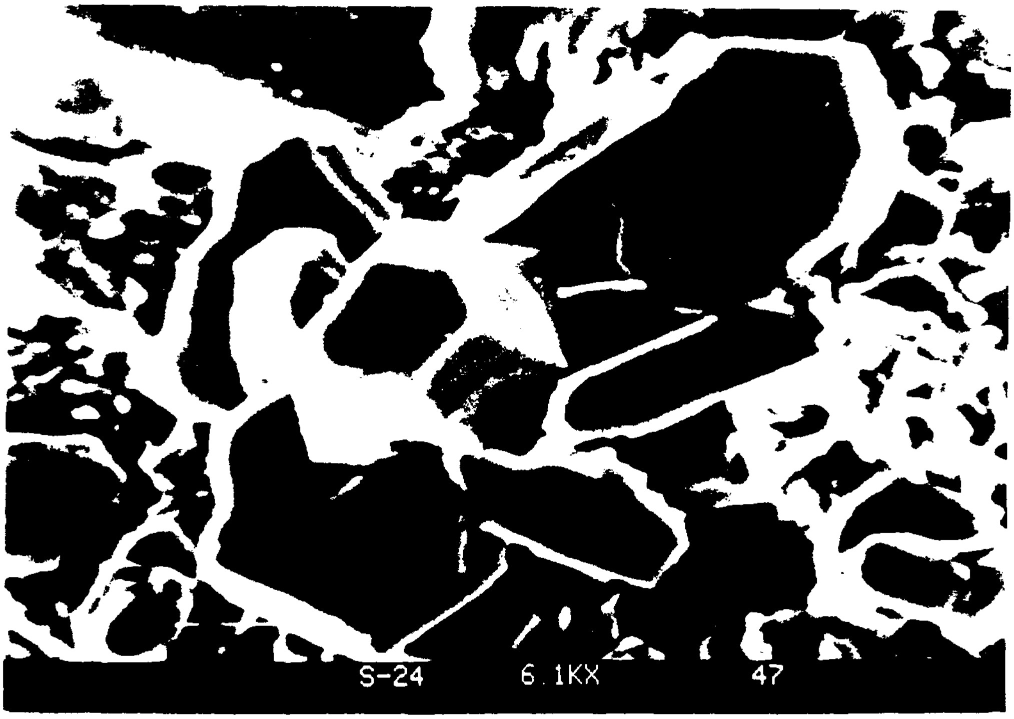

(A) magnification = 6100X

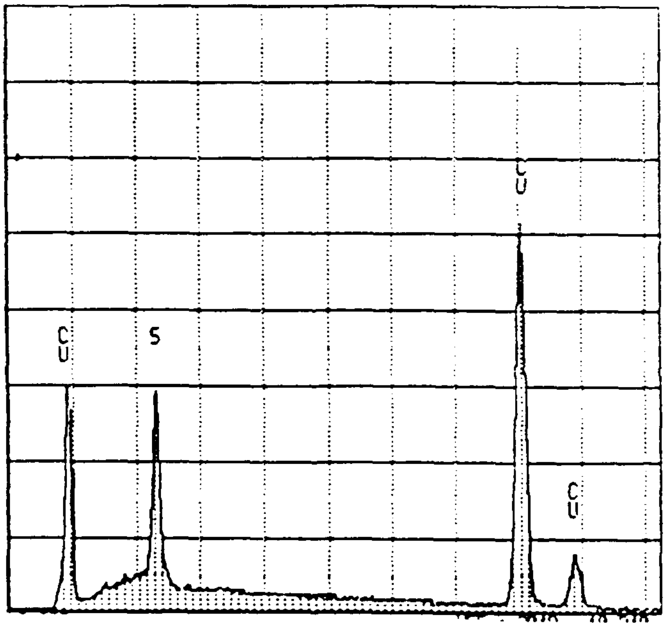

(C)

Figure 5. (A)SEM photomicrograph and (B)EDX analysis of tabular to dipyramidal pseudo-hexagonal phase.

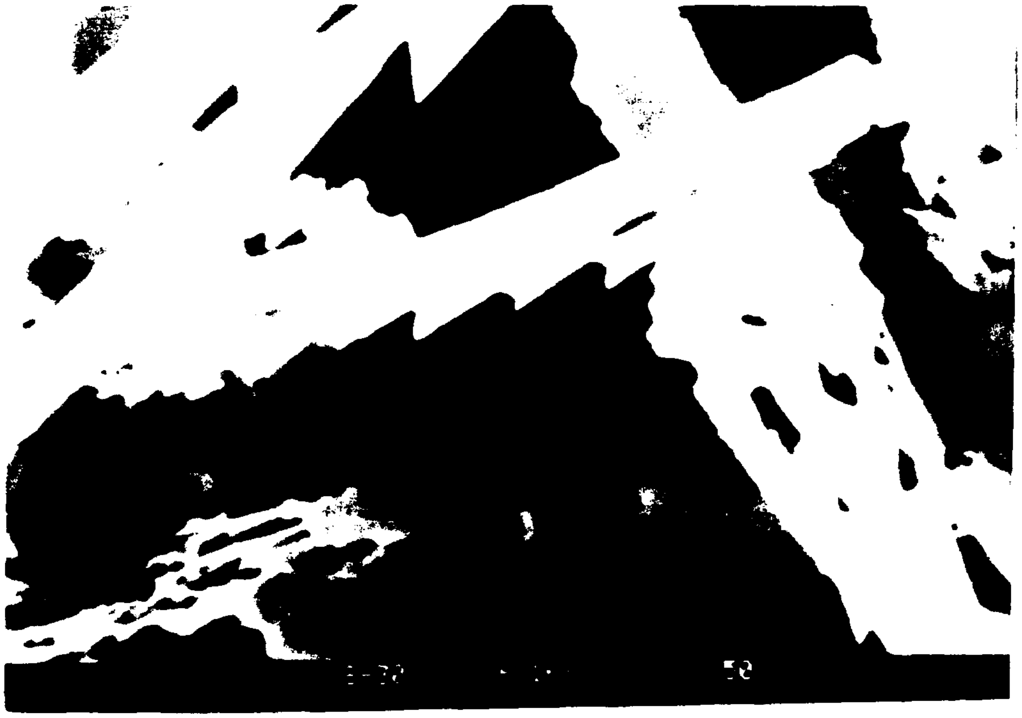

(A) magnification = 6100X

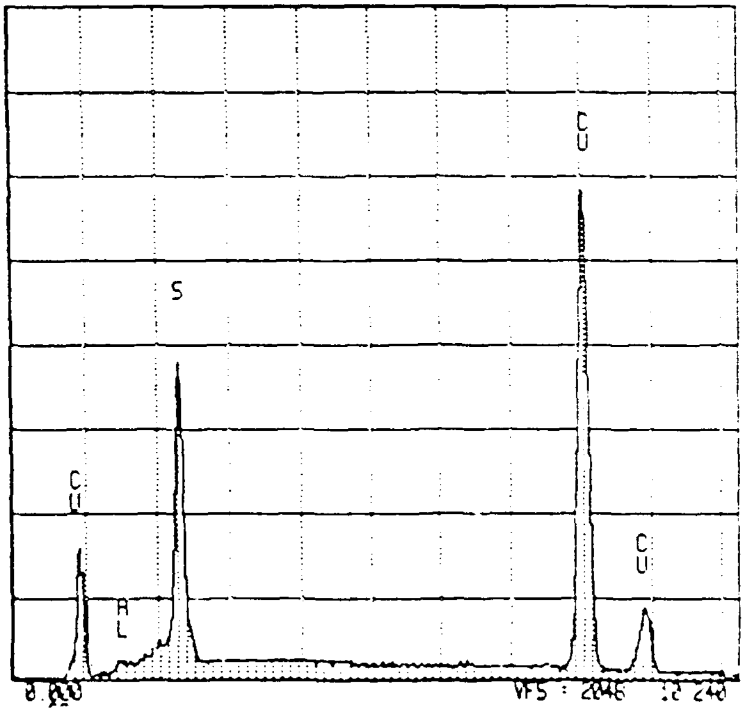

(B)

Figure 6 . (A) SEM photomicrograph (B) EDX analysis of chalcocite occurring as platy elongate crystal with serrated edges.

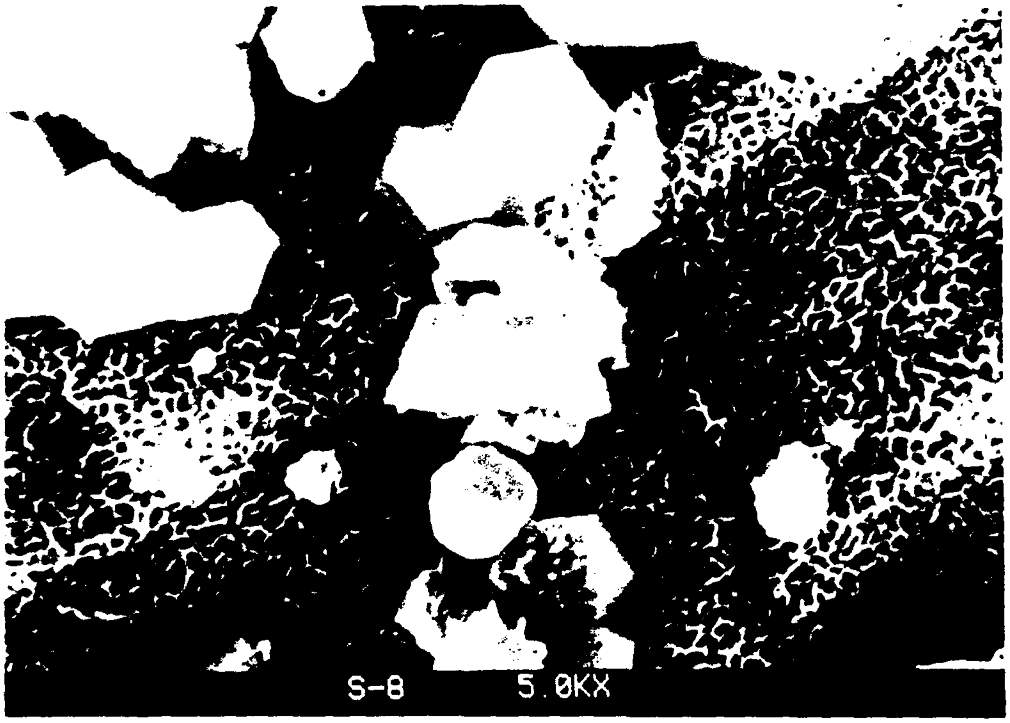

(A) magnification = 5000X

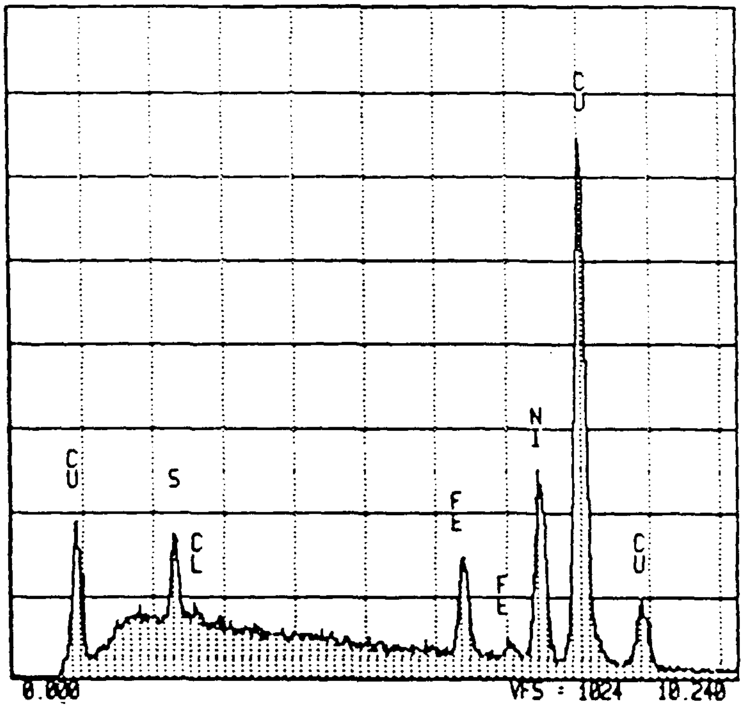

(B)

Figure 7. (A) SEM photomicrograph and (B) EDX analysis of platy, porous Cu, Ni, S and Fe rich layer.

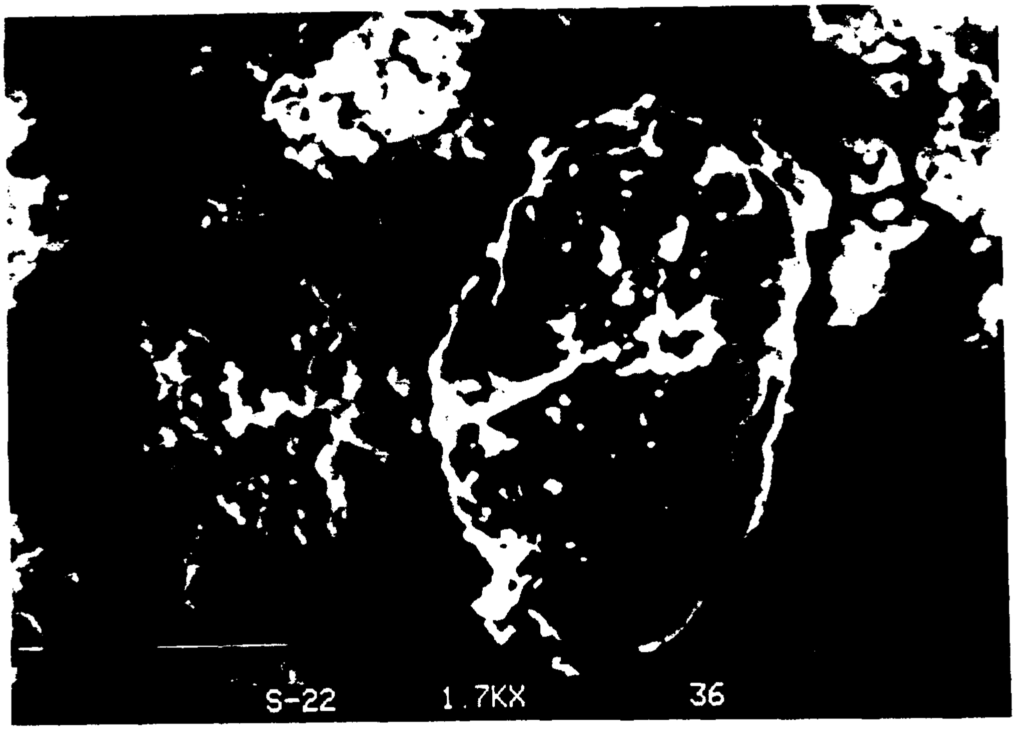

(A) magnification = 1700X

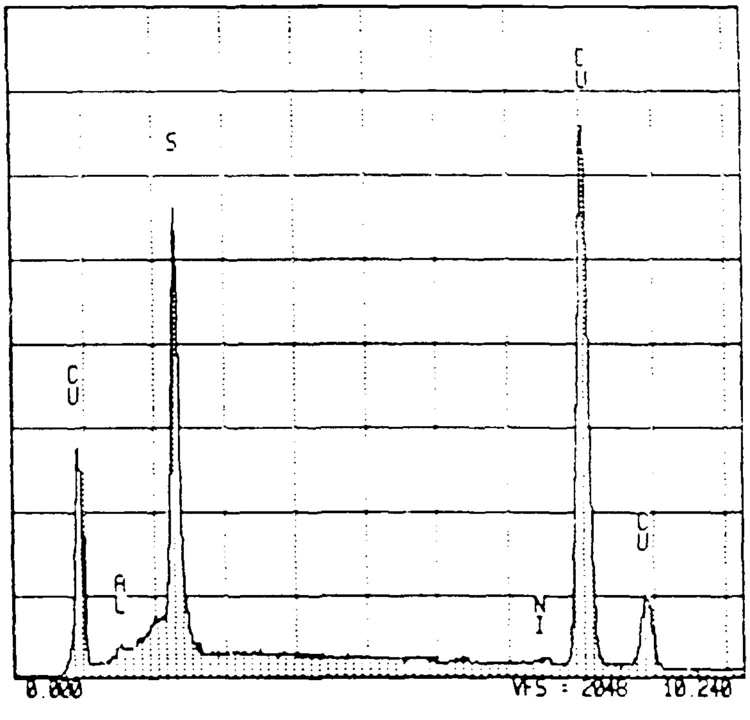

(B)

Figure 8. (A) SEM photomicrograph and (B) EDX analysis of irregularly shaped masses of Cu_2S doped with Ni and minor amounts of Fe.

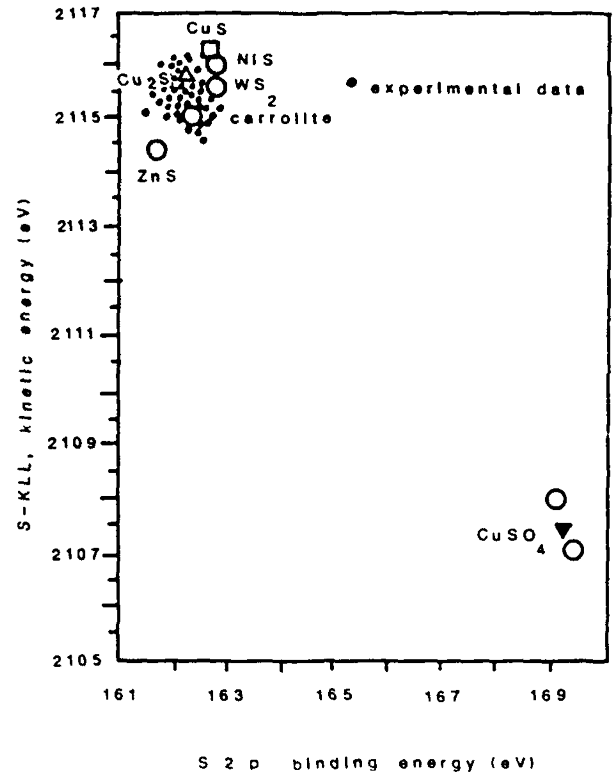

FIGURE 9 - Two-dimensional chemical state plot of S-containing standards and experimental data collected on corroded 90Cu-10Ni wafers.

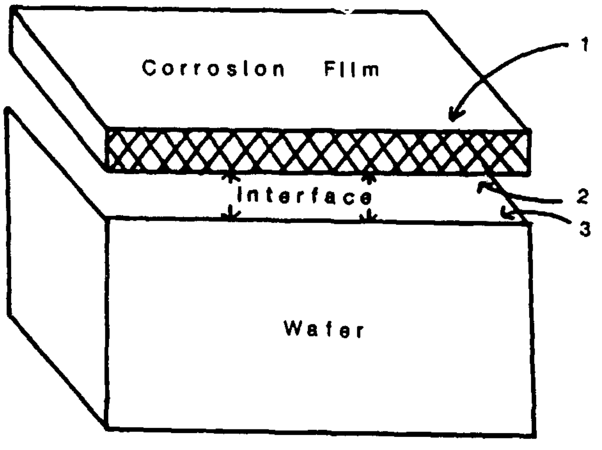

FIGURE 10A - Orientation diagram for ion-etching profile of sample 6 (shown in Figure 10B).

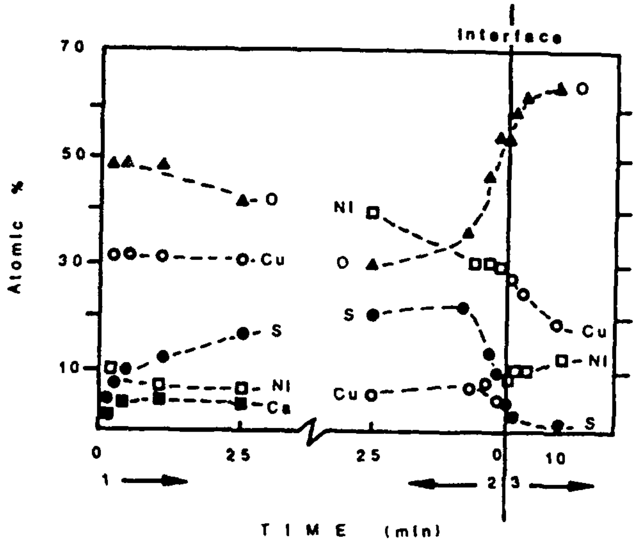

FIGURE 10B - XPS ion-etching profile of sample 6 showing depth dependence of elemental distribution. Points 1 and 2 are respectively, the upper and lower surfaces of the corrosion film and point 3 is the upper surface of the Cu-Ni wafer.

Figure 11A

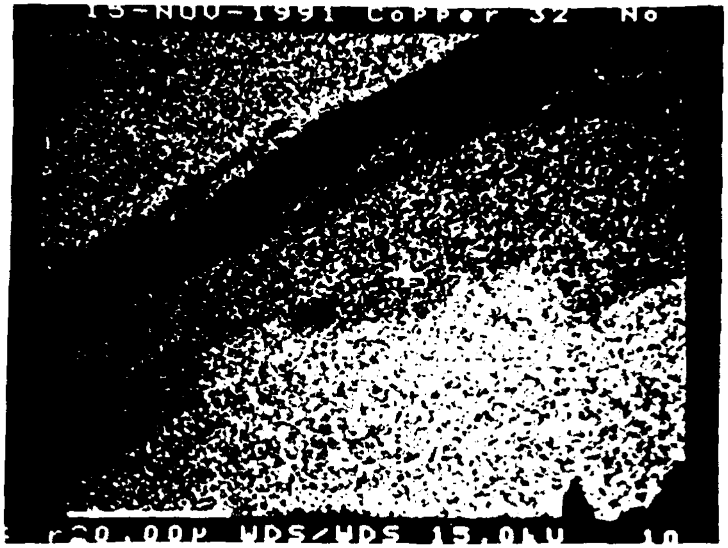

Figure 11B

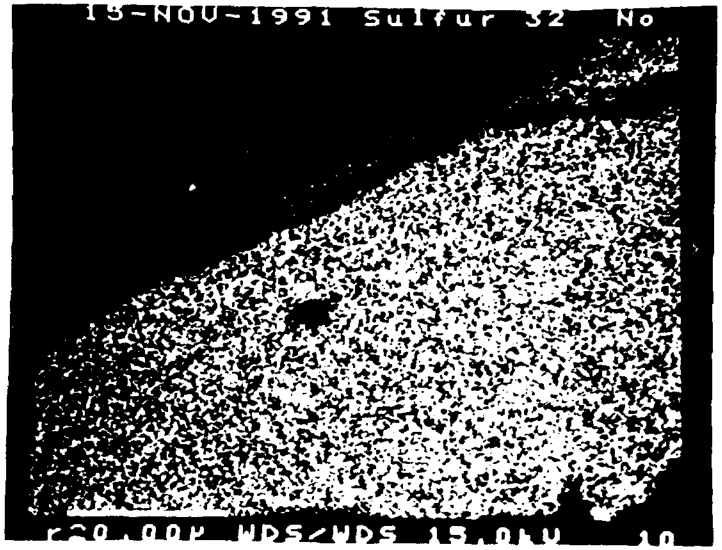

Figure 11C

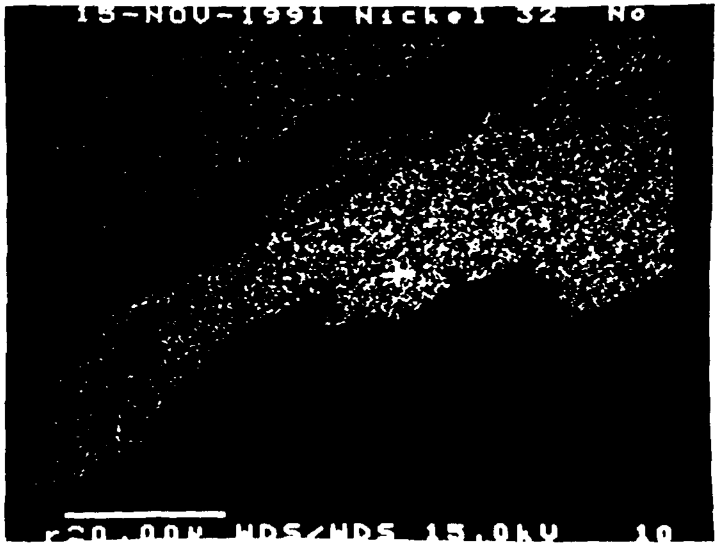

Figure 11D

Figure Captions for Figure 11

A. Back scatter electron image of cross-section of corrosion film found on sample 32. Cu-Ni wafer is seen to the upper left and the outside edge of the corrosion film is to the lower right. The black strip cutting diagonally across the image is an area where the corrosion film separated from the wafer, and is mainly epoxy.

B. X-ray element map of region shown in Figure 11A. The map indicates the distribution of Cu. The light region in the lower right contains the highest concentration of copper in the corrosion film.

C. X-ray element map of region shown in Figure 11A. The map indicates the distribution of S. S is homogenously distributed over the region pictured.

D. X-ray element map of region shown in Figure 11A. The map indicates the distribution of Ni. Ni is virtually absent from the region in the lower right.

For Figures 11B, 11C, and 11D the greater the density of white dots, the higher the concentration of the indicated element.

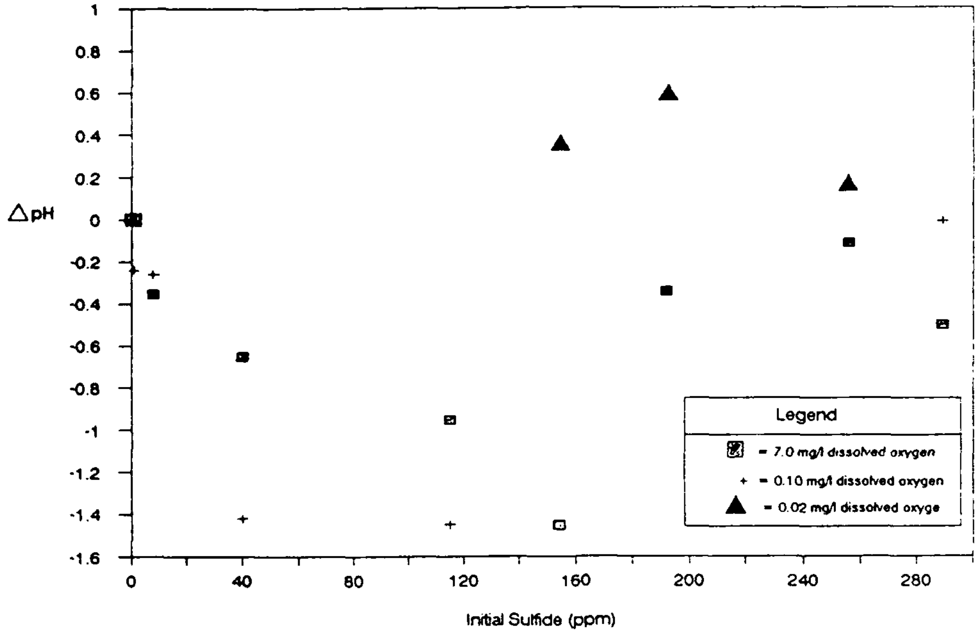

FIGURE 12 - Plot of the magnitude of the change in pH observed in the experimental solutions versus the initial dissolved sulfide content of those solutions.

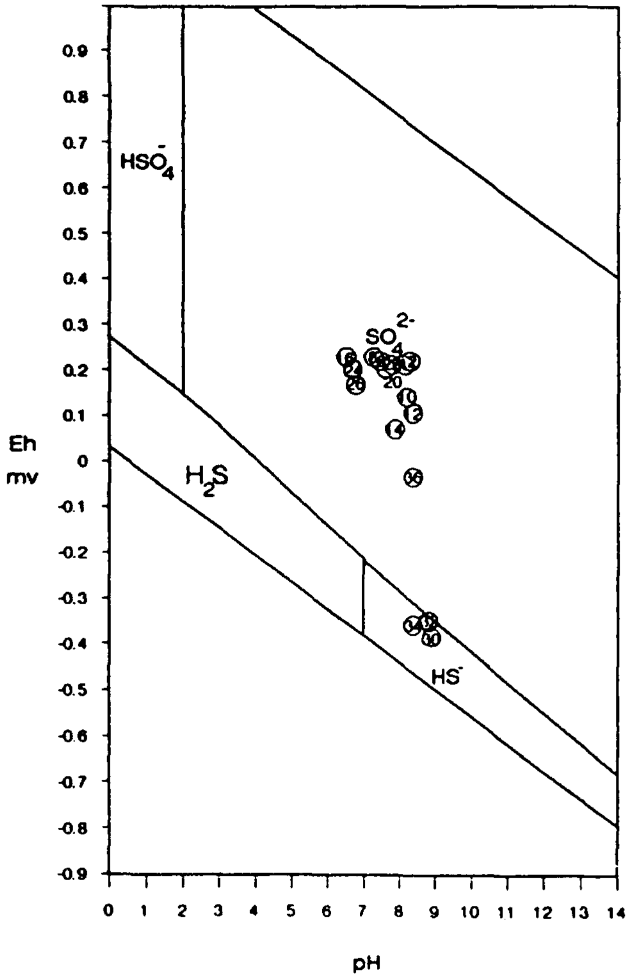

FIGURE 13 - Eh-pH diagram of the aqueous sulfur species showing the final Eh-pH values of the experimental solutions. Stability boundaries are drawn assuming equal activities of the species.

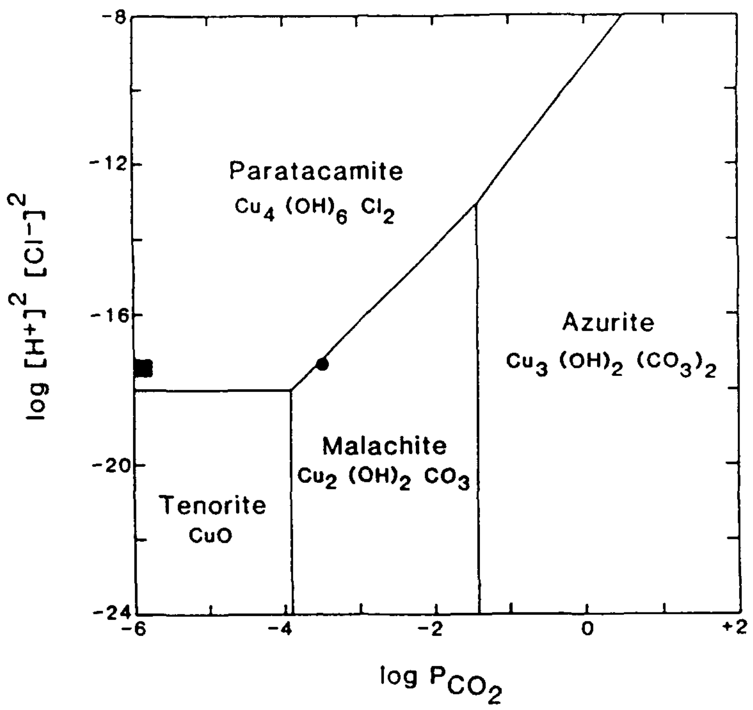

FIGURE 14 - Activity diagram for copper carbonate and chloride minerals likely to occur in the experimental solutions containing high levels of dissolved oxygen and/or low levels of dissolved sulfide. Parameters graphed are the logarithm of the activity product of hydrogen and chloride ion versus the logarithm of the pressure of CO_2 gas. The dot shows the composition of the aerated solutions and the square that of the deaerated and partially deaerated solutions. Log PCO_2 of the latter solutions is estimated.

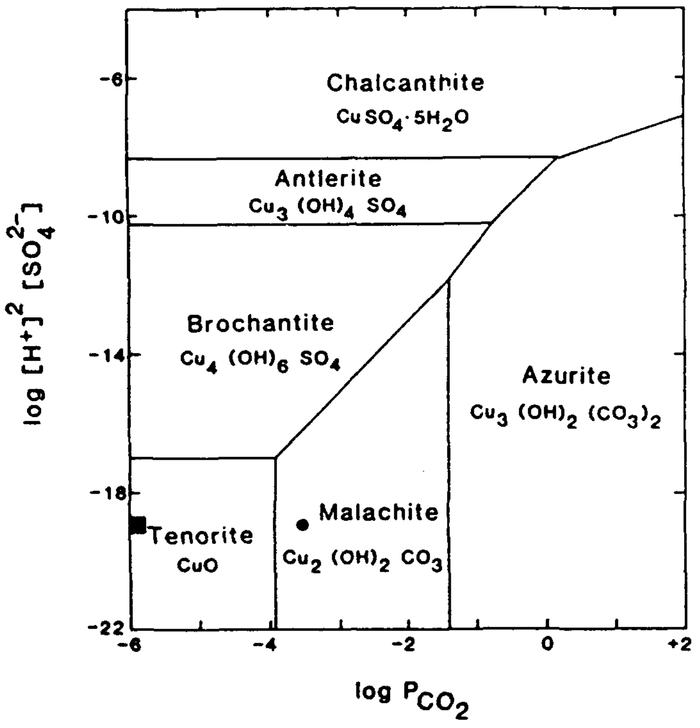

FIGURE 15 - Activity diagram for copper carbonate and sulfate minerals likely to occur in the experimental solutions containing high levels of dissolved oxygen and/or low levels of dissolved sulfide. Parameters graphed are the logarithm of the activity product of hydrogen and sulfate ion versus the logarithm of the pressure of CO_2 gas. The dot shows the composition of the aerated solutions and the square that of the deaerated and partially deaerated solutions. Log PCO_2 of the latter solutions is estimated.

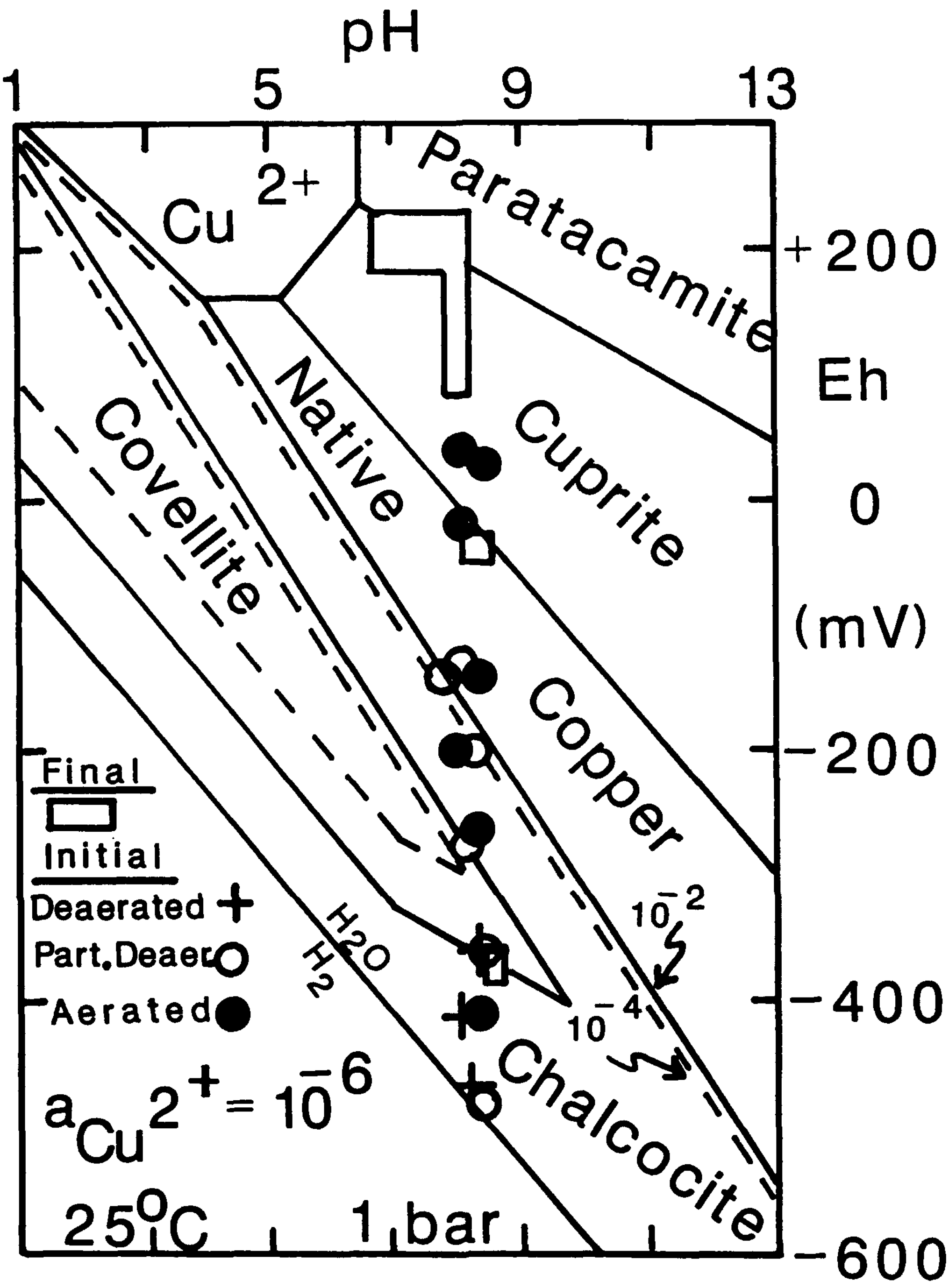

Figure 16. Eh - pH diagram of copper oxide, chloride, and sulfides. The diagram was constructed for 25°C and 1 bar. To construct this and the following two diagrams, the reactions occurring at the phase boundaries were written involving the dominant sulfur species for those Eh-pH conditions. The solid and dashed boundaries were drawn assuming the activity of the aqueous sulfur species to be 10^{-2} and 10^{-4} mol/L, respectively, and the activity of the cupric ion to be 10^{-6}. Final and initial solution compositions are plotted with different symbols and the oxygen contents of the initial solutions are indicated.

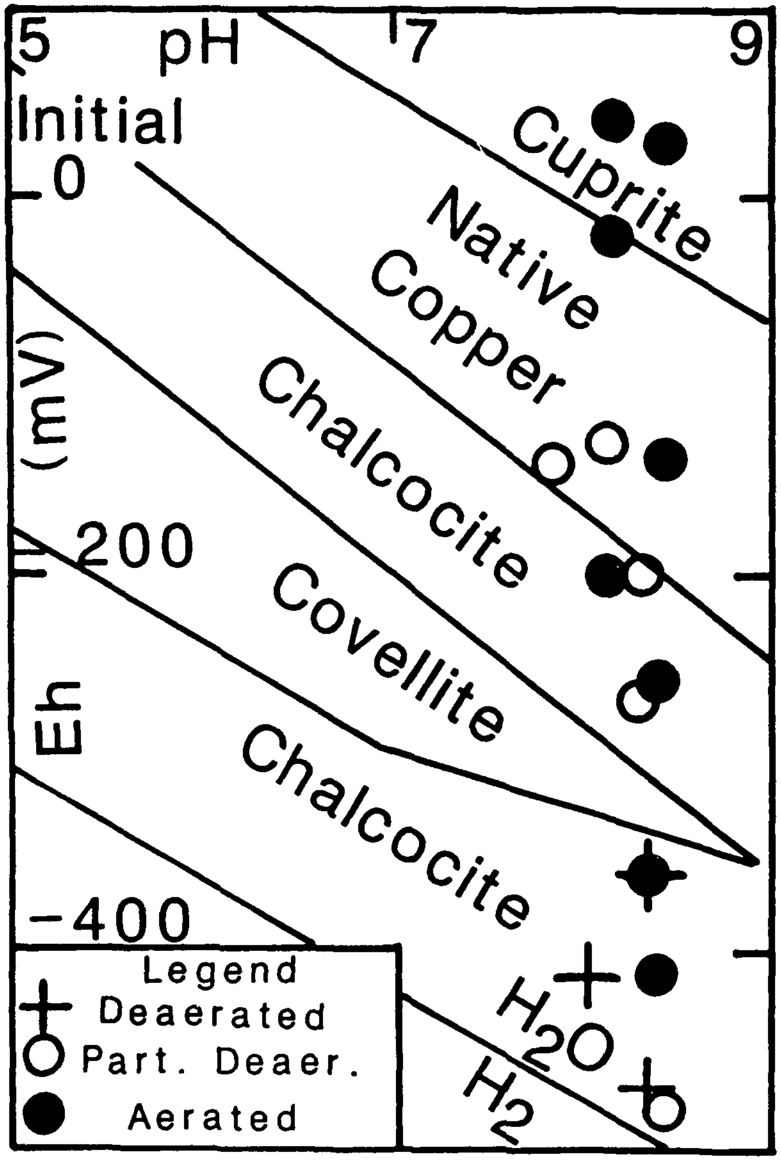

Figure 17. Eh-pH diagram of common copper corrosion products at 25°C and 1 bar. Phase boundaries are drawn assuming activities of the dissolved sulfur species and cupric ion to be 10^{-3} and 10^{-6}, respectively. The compositions of the initial experimental solutions are plotted.

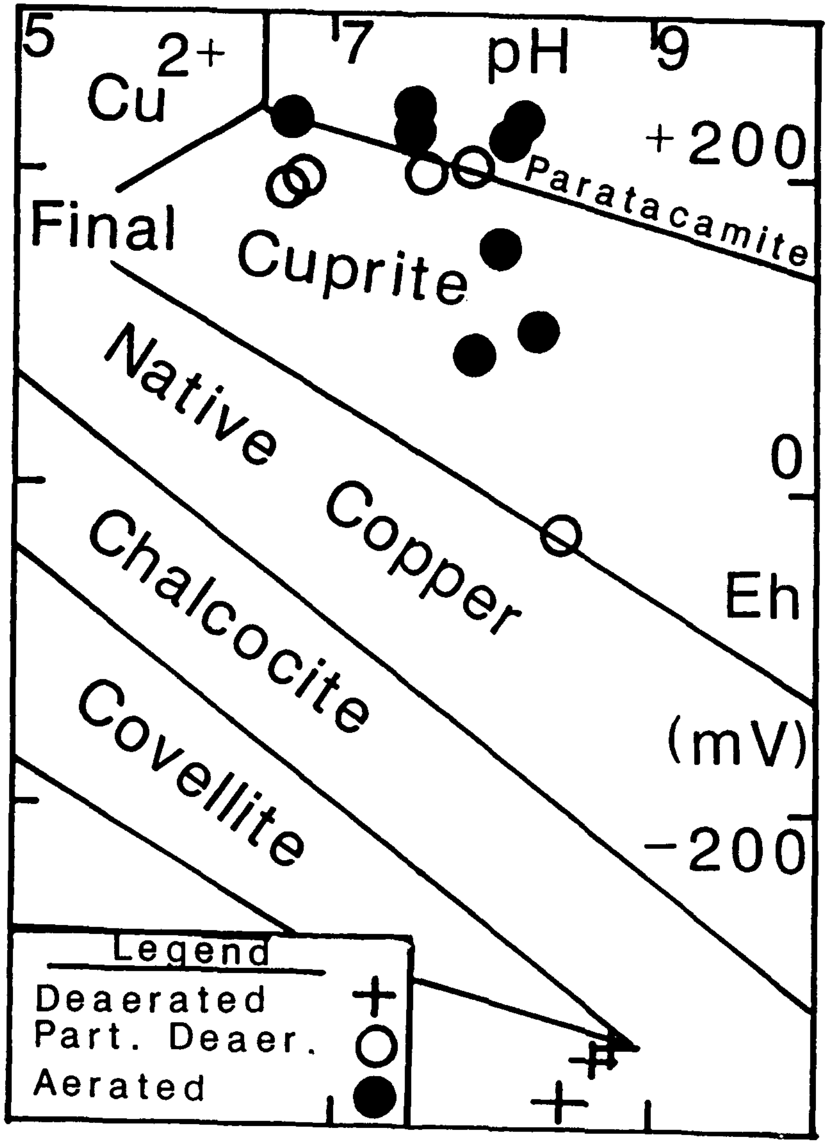

Figure 18. Eh-pH diagram of common copper corrosion products at 25°C and 1 bar. Phase boundaries are drawn assuming activities of the dissolved sulfur species and cupric ion to be 10^{-3} and 10^{-6}, respectively. The compositions of the final experimental solutions are plotted.